

# XMM-Newton study of the Draco dwarf spheroidal galaxy<sup>★</sup>

Sara Saeedi<sup>1</sup>, Manami Sasaki<sup>1</sup>, and Lorenzo Ducci<sup>1,2</sup>

<sup>1</sup> Institut für Astronomie und Astrophysik, Kepler Center for Astro and Particle Physics, Eberhard Karls Universität Tübingen, Sand 1, 72076 Tübingen, Germany  
e-mail: saeedi@astro.uni-tuebingen.de

<sup>2</sup> ISDC Data Center for Astrophysics, Université de Genève, 16 Chemin d'Ecogia, 1290 Versoix, Switzerland

Received 31 March 2015 / Accepted 2 October 2015

## ABSTRACT

**Aims.** We present the results of the analysis of five *XMM-Newton* observations of the Draco dwarf spheroidal galaxy (dSph). The aim of the work is the study of the X-ray population in the field of the Draco dSph.

**Methods.** We classified the sources on the basis of spectral analysis, hardness ratios, X-ray-to-optical flux ratio, X-ray variability, and cross-correlation with available catalogues in X-ray, optical, infrared, and radio wavelengths.

**Results.** We detected 70 X-ray sources in the field of the Draco dSph in the energy range of 0.2–12 keV and classified 18 AGNs, 9 galaxies and galaxy candidates, 6 sources as foreground stars, 4 low-mass X-ray binary candidates, 1 symbiotic star, and 2 binary system candidates. We also identified 9 sources as hard X-ray sources in the field of the galaxy. We derived the X-ray luminosity function of X-ray sources in the Draco dSph in the 2–10 keV and 0.5–2 keV energy bands. Using the X-ray luminosity function in the energy range of 0.5–2 keV, we estimate that  $\sim 10$  X-ray sources are objects in the Draco dSph. We have also estimated the dark matter halo mass that would be needed to keep the low-mass X-ray binaries gravitationally bound to the galaxy.

**Key words.** galaxies: individual: Draco dwarf spheroidal galaxy – X-rays: galaxies – X-rays: binaries

## 1. Introduction

Dwarf spheroidal galaxies (dSphs) are the most numerous galaxies in the Local Group. So far, 19 dSphs satellite galaxies of the Milky Way and 12 of M31 have been detected (Metz & Kroupa 2007). The dSphs are approximately spherical, have no gas or recent star formation, and are usually 1–2 orders of magnitude fainter than the faintest spiral galaxies known (Nucita et al. 2013). They are the least luminous galaxies and their nature is fundamentally different from spiral and elliptical galaxies (Kormendy 1985). The absolute magnitude of dSphs is  $\sim 8$ –12 mag and their optical radius is  $\sim 0.5$ –3 kpc (Irwin & Hatzidimitriou 1995). It has been suggested that dwarf galaxies are the galaxies that are the most dominated by dark matter since their stellar velocity dispersion is significantly larger than would follow from the virial theorem for the luminous mass (Mashchenko et al. 2006).

The Draco dSph (RA = 17h20m19s, Dec =  $57^{\circ}54'55''$ , J2000) has a major and minor diameter of 35'.5 and 24'.5 corresponding to 0.85 and 0.59 kpc (Falco et al. 1999) at a distance of  $82.4 \pm 5.8$  kpc (Kinemuchi et al. 2008). The age is  $\sim 10^{10}$  yr (Aparicio et al. 2001; Bellazzini et al. 2002) and the metallicity of the galaxy is  $Z = 0.0004$  (Girardi et al. 2004), which is  $\sim 0.03$  times the solar value (Caffau et al. 2010). The King model (King 1962) fits the stellar density profile with a core radius of 7'.7 and a tidal radius of 40'.1 (Odenkirchen et al. 2001). Deep photometric surveys show that central stellar density increases inward from  $\sim 2'$  to 0'.5 (Sérgall et al. 2007).

In X-ray surveys, the Draco dSph was first observed by the ROSAT all-sky survey (Voges et al. 1999, 2000) and *Chandra*

(Evans et al. 2010) before the *XMM-Newton* observations were performed. All of the X-ray source studies using the ROSAT or *Chandra* observations were aimed at classifying active galactic nuclei (AGNs) in the field of the Draco dSph (e.g. Gibson & Brandt 2012; Suchkov et al. 2006). In addition, the background X-ray emission of this galaxy in *XMM-Newton* and *Chandra* observations has been studied in order to find evidence for the decay of dark matter (e.g. Riemer-Sørensen & Hansen 2009; Malyshev et al. 2014). Recently, two groups reported the detection of a line at 3.5 keV based on observations of galaxies and galaxy clusters, which was interpreted as a dark matter decay line (Bulbul et al. 2014; Boyarsky et al. 2014). Lovell et al. (2015) have performed simulations of the flux of the dark matter decay line and suggest that an observation of Draco dSph with *XMM-Newton* with a total exposure time of 1.3 Ms is necessary to detect such a line.

This paper reports the results of the study of five *XMM-Newton* observations of the Draco dSph and is organised as follows. In Sect. 2 we describe the data reduction and analysis of the *XMM-Newton* observations. In Sect. 3 we present the different methods used to classify the X-ray sources. In Sect. 4 we explain the properties and the classification of the detected sources. In Sect. 5 we discuss the X-ray luminosity function and the possible presence of low-mass X-ray binaries in the Draco dSph.

## 2. Reduction and data analysis

We analysed the public archival *XMM-Newton* (Jansen et al. 2001) observations of the Draco dSph. Table 1 summarises the details of the observations. All observations were pointed approximately at the centre of the galaxy (RA = 17h20m12.40s, Dec =  $+57^{\circ}54'55''.3$ , J2000). In all observations, the European

<sup>★</sup> Based on observations obtained with *XMM-Newton*, an ESA science mission with instruments and contributions directly funded by ESA Member States and NASA.

**Table 1.** *XMM-Newton* observations of the Draco dSph.

ID <sup>†</sup>	Observation ID	Observation date	EPIC-pn		EPIC-MOS1		EPIC-MOS2	
			mode/filter*	<i>T.exp</i> [ks]*	mode/filter*	<i>T.exp</i> [ks]*	mode/filter*	<i>T.exp</i> [ks]*
OBS1	0603190101	2009-Aug.-04	FF/Thin1	17.0	FF/Thin1	18.6	FF/Thin1	18.6
OBS2	0603190201	2009-Aug.-06	FF/Thin1	18.0	FF/Thin1	19.4	FF/Thin1	16.4
OBS3	0603190301	2009-Aug.-08	FF/Thin1	12.5	FF/Thin1	12.7	FF/Thin1	12.8
OBS4	0603190401	2009-Aug.-20	FF/Thin1	3.1	FF/Thin1	9.3	FF/Thin1	7.2
OBS5	0603190501	2009-Aug.-28	FF/Thin1	18.0	FF/Thin1	19.6	FF/Thin1	19.6

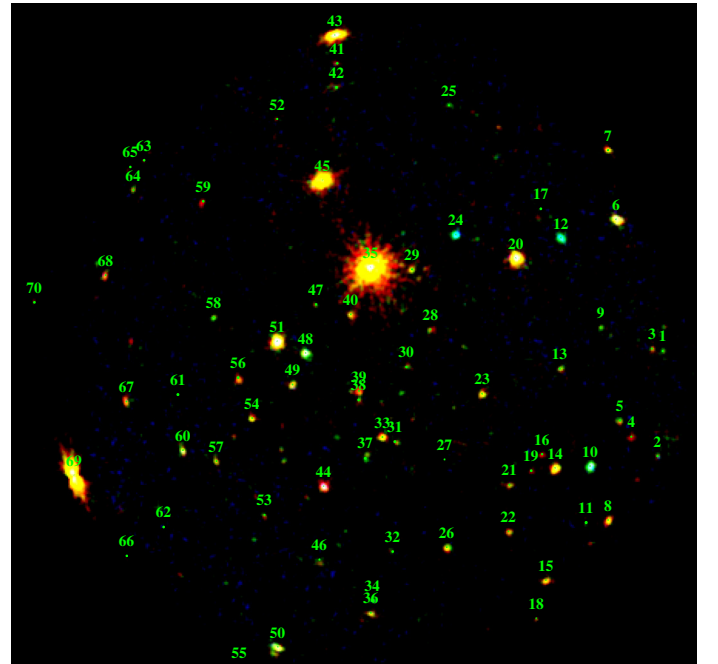
**Notes.** (<sup>†</sup>) ID numbers used in the text; (\*) FF: full frame; (<sup>\*</sup>) *T.exp*: exposure time after screening for high background.

Photo Imaging Cameras EPIC-pn (Strüder et al. 2001) and EPIC-MOS1/2 (Turner et al. 2001) were operated in the full-frame mode with a time resolution of 73.4 ms and 2.6 s, respectively.

The data analysis was performed using the *XMM-Newton* Science Analysis System (SAS<sup>1</sup>) version 11.0.1. For each observation, we produced EPIC-pn and EPIC-MOS event files via the `emchain` and `epchain` tools. Good-time intervals (GTIs) were determined for each EPIC by screening for time intervals with high-energy background caused by soft proton flares. In OBS4, the MOS data were broken into two parts due to the flares. We merged the event files and extracted GTIs. Owing to the long duration of the high background proton flares in this observation, the exposure time is significantly lower than in the other observations (see Table 1).

For each observation, the data were split into five energy bands: B1 (0.2–0.5 keV), B2 (0.5–1.0 keV), B3 (1.0–2.0 keV), B4 (2.0–4.5 keV), and B5 (4.5–12 keV). Single to quadruple pixel events (`PATTERN` ≤ 12) have been used for all five energy bands of the EPIC-MOS data. In the EPIC-pn data, only single-pixel events (`PATTERN` = 0) were used for the first energy band, and for the other energy bands single and double-pixel events (`PATTERN` ≤ 4) were used. We also applied `FLAG` = 0 to reject all events that were close to CCD gaps or on bad pixels. We produced images in five energy bands for each observation and EPIC. In addition, we produced mosaic images that were a combination of all observations using EPIC images, in all sub-bands, and in the total energy band of 0.3–12.0 keV. A three-colour image of the mosaic images is shown in Fig. 1.

In the process of source detection, we ran the SAS task `edetect-chain` for each observation in five energy bands for the three EPIC detectors separately and also for the total energy band mosaic image. In the source detection steps, we selected a minimum detection likelihood of 10 as the threshold for the primary detection of the sources<sup>2</sup>. We kept the `boxsize` with the default value of 5 pixels for accumulating the source counts to create a list of source positions, which is used to create background maps by excluding the events at these positions. A two-dimensional spline was fitted to the exposure-corrected image. We used 16 default spline nodes. In the next step, source detection was performed using the background maps, assuming a default minimum detection likelihood of 8. Finally, for all energy bands of each EPIC, a maximum likelihood point-spread function (PSF) was fitted to the source count distribution at the



**Fig. 1.** Logarithmically scaled mosaic three-colour image of the *XMM-Newton* observations in the field of the Draco dSph. The images are smoothed with a 2D Gaussian with a kernel radius of 1.5 pixels. The colours represent the energy range of red: 0.3–1.0 keV, green: 1.0–2.0 keV, and blue: 2.0–12 keV. Detected sources are marked with the number of sources in final catalogue (see Appendix A).

position of the new detections and the final source list was created for each EPIC with a higher threshold for the maximum detection likelihood of 10. In each observation, we detected about 60–65 sources with EPIC-pn and 15–25 with MOS1/2. Each observation is subject to spurious detections, which are produced by systematic effects of the instruments and detection software. As Saxton et al. (2008) have shown, ~4% of the detections in the EPIC-pn data with  $ML > 10$  are false detections. We minimised the number of spurious sources by checking each image by eye and comparing the source detection results of all EPICs and all observations. In total, we removed eight spurious sources from the source list (see next section).

## 2.1. Source catalogue

Since we performed source detection separately for all observations for each EPIC and each energy band, we had to combine the results to obtain a final source catalogue. First, we examined each list of detections by visual inspection and removed

<sup>1</sup> <http://xmm.esac.esa.int/sas/>

<sup>2</sup> The detection likelihood is calculated by the probability of Poisson random fluctuation of the counts. This probability is calculated on the basis of the raw counts of the source and the raw counts of the background maps.

**Table 2.** Energy conversion factors (ECFs) for each EPIC energy band.

Energy band	EPIC-pn	EPIC-MOS
B1 (0.2–0.5 keV)	1.12e+12	1.79e+11
B2 (0.5–1.0 keV)	9.05e+11	1.91e+11
B3 (1.0–2.0 keV)	5.72e+11	2.05e+11
B4 (2.0–4.5 keV)	1.98e+11	7.73e+10
B5 (4.5–12 keV)	5.59e+10	1.54e+10

the spurious sources caused by bad pixels, hot columns, gaps, or edges of the CCD chips as well as background fluctuations. After all the artefacts had been removed, the source lists of all observations for all EPICs and all five energy bands were combined into one source list.

The final catalogue includes 70 sources in the field of the Draco dSph. For each of the detected sources, we derived the X-ray flux  $F_i$  (in units of  $\text{erg s}^{-1} \text{cm}^{-2}$ ) in each energy band ( $i$ ) using the relation

$$F_i = \frac{B_i}{\text{ECF}_i}, \quad (1)$$

where  $B_i$  is the count-rate and  $\text{ECF}_i$  is the energy conversion factor, which was calculated according to the recent calibration matrices of EPIC-MOS and EPIC-pn. We obtained the ECF by assuming a power-law model with the Galactic foreground absorption of  $N_{\text{H}} = 2.46 \times 10^{20} \text{cm}^{-2}$  (Willingale et al. 2013) and a photon index of  $\Gamma = 1.81$ , which is obtained by fitting a power-law model to the spectra of the hard sources (see Sect. 3.3). Table 2 lists the values of the ECFs for each EPIC energy band.

The faintest detected source in the field of the Draco dSph, classified neither as a foreground nor as a background object, is source No. 28 with a luminosity of  $(3.94 \pm 1.69) \times 10^{33} \text{erg s}^{-1}$ . Appendix A lists the position of each source, the count rate, total weighted flux, detection likelihood, and hardness ratios in different energy bands (see Sect. 3.4).

## 2.2. Astrometrical corrections

To reduce the uncertainties of the position of the X-ray sources, we compared the measured positions of sources that were detected in more than one observation. If the positions of these sources were closer than the combined  $3\sigma$  statistical errors in different observations, we considered them to be one source. We checked the difference between the RA and Dec of OBS 2, 3, 4, and 5 with respect to OBS1 to see if there is a shift in the position of sources. No significant offset was measured.

As the optical astrometry is more accurate, we selected 14 bright X-ray sources that had counterparts in the SDSS9 survey (Ahn et al. 2012) and compared their positions with those of the optical counterparts. The error of the X-ray positions of the *XMM-Newton* observations is estimated by the weighted mean of the  $\Delta\text{RA}$  and the  $\Delta\text{Dec}$  between the positions of the optical and X-ray sources. Table 3 shows the RA and Dec position offsets of EPIC-MOS1, EPIC-MOS2, and EPIC-pn from the optical position for the five observations and the mosaic image. The final selected coordinates of each X-ray source, given in Appendix A, is the corrected position of that observation that has the best statistical maximum likelihood.

## 2.3. Cross-correlation with other catalogues

In the first step of identifying X-ray sources in the field of the Draco dSph, we searched for correlation of X-ray sources with

**Table 3.** Offsets of the different *XMM-Newton* observations of the Draco dSph.

OBS-ID	EPIC	$\Delta\text{RA} (")$	$\Delta\text{Dec} (")$
OBS1	PN	$-0.09 \pm 0.01$	$0.03 \pm 0.01$
	MOS1	$-0.18 \pm 0.03$	$-0.07 \pm 0.03$
	MOS2	$-0.23 \pm 0.02$	$-0.014 \pm 0.02$
OBS2	PN	$-0.10 \pm 0.01$	$-0.13 \pm 0.01$
	MOS1	$-0.06 \pm 0.03$	$-0.15 \pm 0.03$
	MOS2	$-0.12 \pm 0.02$	$-0.09 \pm 0.02$
OBS3	PN	$-0.22 \pm 0.02$	$-0.08 \pm 0.02$
	MOS1	$-0.23 \pm 0.05$	$-0.08 \pm 0.05$
	MOS2	$-0.22 \pm 0.04$	$0.04 \pm 0.04$
OBS4	PN	$0.05 \pm 0.08$	$-0.15 \pm 0.08$
	MOS1	$0.11 \pm 0.05$	$-0.07 \pm 0.05$
	MOS2	$0.05 \pm 0.07$	$-0.08 \pm 0.07$
OBS5	PN	$0.03 \pm 0.01$	$-0.07 \pm 0.01$
	MOS1	$0.09 \pm 0.06$	$0.06 \pm 0.06$
	MOS2	$-0.06 \pm 0.03$	$-0.02 \pm 0.03$
MOSAIC		$-0.035 \pm 0.002$	$-0.030 \pm 0.002$

sources in published catalogues. We searched for counterparts within the radius of  $3 \times \sqrt{\sigma_{\text{stat}}^2 + \sigma_{\text{sys}}^2}$  in catalogues of different wavelengths of the VIZIER<sup>1</sup> and SIMBAD<sup>2</sup> archives. The value of  $\sigma_{\text{stat}}$  is the statistical error of X-ray source detection, and  $\sigma_{\text{sys}}$  includes the positional error of the correlated source and the uncertainty of the offset between the optical and X-ray position. In optical and infrared catalogues, we ignored  $\sigma_{\text{sys}}$  because it is significantly lower than the  $\sigma_{\text{stat}}$  of the X-ray sources. The positional uncertainties were either taken from the respective catalogues or from the technical data of the telescopes. Sources are considered to be counterparts if their positions overlap within the  $3\sigma$  positional error (Watson et al. 2009; Rutledge et al. 2000). In the following, the catalogues that were used for the cross-correlation are listed:

**Milky Way stars catalogue:** the GALEX catalogue of UV sources (Bianchi et al. 2011) includes a catalogue of hot stars and white dwarfs that belong to the Milky Way. The positional error of the sources was  $\sim 0.5$ .

**AGN catalogues:** we used the most updated catalogues of AGNs covering the field of the Draco dSph: the quasars and active galactic nuclei catalogue (13th edn., Veron-Cetty & Veron 2010b), the QSO candidates selection in the virtual observatory era (D’Abrusco et al. 2009), the photometric classification catalogue of SDSS DR7 (Abraham et al. 2012), the large quasar astrometric catalogue 2 (LQAC-2, Souchay et al. 2012), the photometric selection of quasars from SDSS II (Richards et al. 2009), the all-sky atlas of radio/X-ray associations (Flesch 2010), and the quasar catalogue of Kinemuchi et al. (2008) in the field of the Draco dSph.

**The Draco dSph stars catalogues:** there are three catalogues of the Draco dSph stars that used deep photometric studies with the MegaCam camera at the Canada-France-Hawaii Telescope with three different filters ( $g = 487 \text{ nm}$ ,  $r = 625 \text{ nm}$ ,  $i = 770 \text{ nm}$ ), the Wide Field Camera at the *Isaac Newton*

<sup>1</sup> <http://vizier.u-strasbg.fr/viz-bin/VizieR>

<sup>2</sup> <http://simbad.u-strasbg.fr/simbad/>

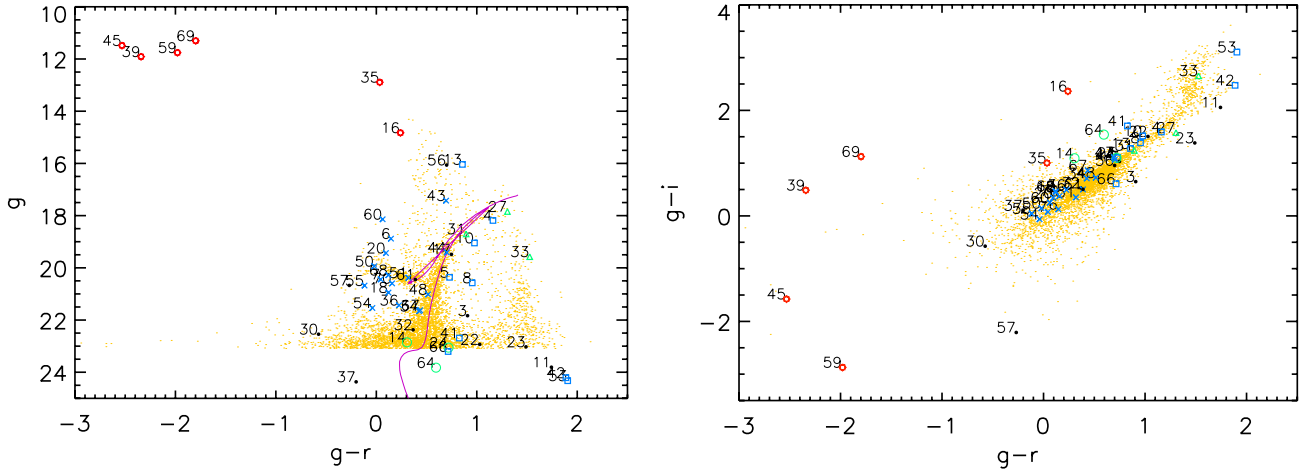


**Fig. 2.** Colour–magnitude (*left*) and colour–colour (*right*) diagrams of the SDSS9 optical counterparts of the X-ray sources. Foreground stars are labelled by red star symbols, AGNs with blue crosses, galaxies with blue squares, X-ray binary candidates with green circles, and other binary systems with green triangles. Unclassified sources are labelled by black dots. Orange dots represent the SDSS7 members ( $g < 23$  mag) of the Draco dSph as classified by Rave et al. (2003). The violet line is the stellar isochrone for the age ( $10^{10}$  yr) and metallicity (0.0004) of the Draco dSph according to Girardi et al. (2004). It is obvious that most of the stars in the galaxy are already on the red giant branch.

Telescope (INT) with standard filters ( $V, I$ ), and the Wide Field and Planetary Camera on board the *Hubble* Space Telescope (HST; Ségall et al. 2007); these catalogues list the members of the Draco dSph based on the analysis of colour–magnitude diagrams for each observation. The positional error of the optical sources is  $\leq 0''.5$ . The HST survey was limited to the centre of the galaxy, where no *XMM-Newton* X-ray source was detected. In the MegaCam and INT catalogues, we generally found more than one counterpart in the  $3\sigma$  error circle of the X-ray sources. Therefore, we selected the brightest optical source as the counterpart. If there were counterparts in other optical or infrared catalogues, we selected the brightest source with consistent magnitudes in similar energy bands of the different catalogues as the counterpart.

For more accuracy, we also considered other catalogues of the Draco dSph in which the members of the galaxy are classified by different methods in different wavelengths. The catalogue of Kleyna et al. (2002) contains a few hundred stars selected by radial velocity. Rave et al. (2003) classified all sources with  $g < 23$  mag of the SDSS7 survey in the field of the Draco dSph as either stars of the galaxy, faint sources, or background galaxies using several photometric methods. The selected members of Draco dSph are consistent with five other previous catalogues. On the basis of the infrared and optical observations, Cioni & Habing (2005) classified late-type stars of the Draco dSph. Piatek et al. (2001) selected the members of the Draco dSph in  $R$  and  $V$  band photometry.

**Optical catalogues:** the SDSS9 catalogue is the 9th released data of the Sloan Digital Sky Survey (Ahn et al. 2012). We selected this catalogue as the main optical reference because it was the most updated survey, and because we had access not only to its images, but also to the apparent magnitudes and errors in five different optical energy bands from near ultraviolet (UV) to near infrared ( $u = 3551 \text{ \AA}$ ,  $g = 4686 \text{ \AA}$ ,  $r = 6165 \text{ \AA}$ ,  $i = 7481 \text{ \AA}$ ,  $z = 8931 \text{ \AA}$ ). Furthermore, the redshifts of the background objects are available for the brightest sources. The positional uncertainty of a source in the SDSS9 catalogue depends on its brightness and is between  $0''.003$  and  $0''.2$  for the sources considered counterparts of the *XMM-Newton* sources. Table A.2 lists the

$g, r, i$  magnitudes of the optical counterparts in SDSS9 catalogue and Fig. 2 shows the colour–magnitude and colour–colour diagrams of the SDSS9 optical counterparts of the X-ray sources.

**Infrared catalogues:** infrared counterparts were found in two catalogues: the WISE All-Sky Data released in four energy bands (3.4, 4.6, 12, and  $22 \mu\text{m}$ , called  $W1, W2, W3,$  and  $W4$ , respectively; Cutri & et al. 2012), and the 2MASS All-Sky Catalogue of Point Sources with  $J, H, K$  filters (Cutri et al. 2003). The positional uncertainty of WISE sources is  $0''.3\text{--}1''$  and the average positional uncertainty of 2MASS is  $\sim 3''$ . Figure 3 shows the colour–magnitude diagrams of the infrared counterparts.

**Radio catalogue:** for radio counterparts, we used the 1.4 GHz NRAO VLA Sky Survey (NVSS, Condon et al. 1998).

**X-ray catalogues:** we found counterparts in the ROSAT all sky bright/faint source catalogues (Voges et al. 1999, 2000) and the *Chandra* catalogue (Evans et al. 2010) for one-third of the brightest sources that were detected in the *XMM-Newton* observations of the Draco dSph. Only a small fraction of the field of view of *XMM-Newton* was observed with *Chandra*. There are 24 sources in the *Chandra* catalogue in this field of the sky and 20 of them have also been detected with *XMM-Newton*. The *Chandra* fluxes are consistent with the average fluxes measured with *XMM-Newton* (see Sect. 3.1.2).

### 3. Analysis

#### 3.1. Variability study

##### 3.1.1. Short-term variability

For sources with counts  $\geq 200$ , we extracted the barycentrically corrected light curves of each source and its background. To search for a possible periodic signal, we used the Lomb-Scargle technique for unevenly sampled time series (Scargle 1982). We studied the Lomb-Scargle periodograms for the 0.2–12 keV light curves of each observation. We could not find any evidence

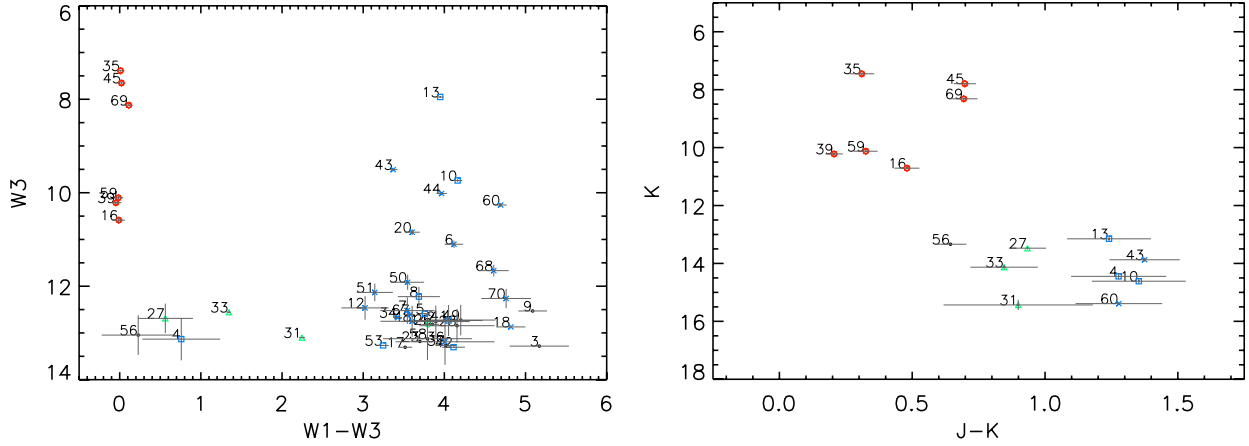


**Fig. 3.** Colour–magnitude diagrams of the infrared counterparts of the *XMM-Newton* sources. *Left*: WISE W2(4.6  $\mu\text{m}$ ) versus the colour index W1 (3.4  $\mu\text{m}$ ) – W3 (12  $\mu\text{m}$ ). *Right*: 2MASS *K* band versus the colour index *J* – *K*. For the different source classes the same symbol types are used as in Fig. 2.

of pulsation or periodicity for the brightest sources (with counts  $\geq 200$ ) in the Draco dSph.

To improve the search for pulsations, especially for the faint sources, we extracted the barycentrically corrected event files of the sources in each observation and EPIC and applied the  $Z_n^2$  analysis (Buccheri et al. 1983, 1988). We checked the periodograms for the first and second harmonics of the photon arrival times of EPIC-pn event files in the energy range of 0.2–12 keV. We found pulsation of source No. 65 in OBS2 (see Sect. 4.3.1).

### 3.1.2. Long-term variability

Since the observations were spread out over two weeks (see Table 1), we also checked the flux variability on long timescales. We calculated the flux of the sources in each observation or the upper limit of the flux at the position of a source in the case that source was not detected. Appendix B shows the long-term light curves of the (0.2–4.5 keV) flux of all sources over five observations. Band 5 (4.5–12 keV) is excluded because it is subject to hard background contamination and low sensitivity both for EPIC-pn and EPIC-MOS.

To compare the 0.2–4.5 keV fluxes between different observations, the ratio (*Var*) of the flux and the significance (*S*) of the difference have been calculated by using two formulae,

$$Var = \frac{F_{\max}}{F_{\min}} \quad (2)$$

$$S = \frac{F_{\max} - F_{\min}}{\sqrt{EF_{\max}^2 + EF_{\min}^2}}, \quad (3)$$

where  $F_{\max}$  and  $F_{\min}$  are the maximum and minimum X-ray flux (or the upper limit), and  $EF_{\max}$  and  $EF_{\min}$  are the errors of the maximum and minimum flux of the source, respectively. The variability factor was calculated for the sources that were detected in at least two observations (see Appendix B). We considered the source as variable if the statistical variability significance (*S*) was higher than 3. Figure 4 shows the variability factor (*Var*) of the sources and the hardness ratio  $HR_3$  (see Sect. 3.4). For sources for which we also have a *Chandra* detection, we included the *Chandra* flux in the long-term light curves. For all these sources, the *Chandra* flux is consistent with the average *XMM-Newton* flux, indicating that none of them show variability

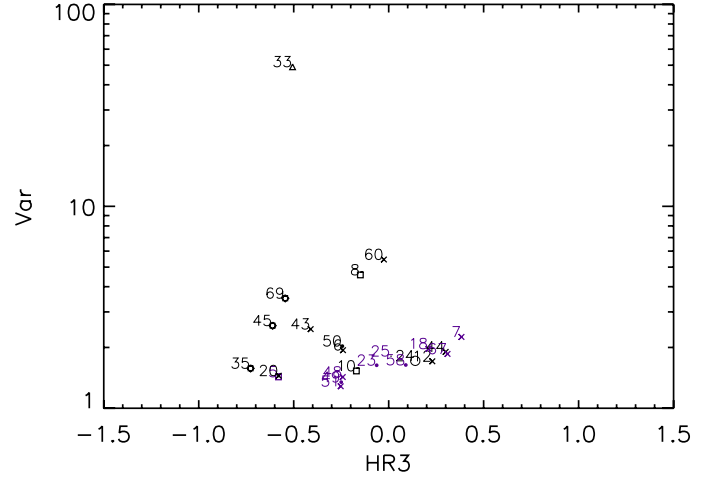


**Fig. 4.** Variability factor of sources in the 0.2–4.5 keV band plotted versus  $HR_3$ . Sources with a statistical significance of variability below 3 are marked in violet. For the different source classes the same symbol types are used as in Fig. 2.

between the *Chandra* and *XMM-Newton* observations. Table 4 gives the fluxes of the *Chandra* sources converted into the used energy band of 0.2–12.0 keV.

### 3.2. X-ray-to-optical flux ratio

A very useful tool for separating optically bright sources (like stars) from X-ray bright sources (like X-ray binaries) is the X-ray-to-optical flux ratio.

For each source associated with an optical source, we modified the equation of Maccacaro et al. (1988) to

$$\log_{10} \left( \frac{F_x}{F_{\text{opt}}} \right) = \log_{10}(F_x) + \frac{g+r}{2 \times 2.5} + 5.37, \quad (4)$$

where the standard band *B* ( $\lambda_{\text{eff}} = 0.43 \mu\text{m}$ ) and *R* ( $\lambda_{\text{eff}} = 0.65 \mu\text{m}$ ) were replaced by the *g* band ( $\lambda_{\text{eff}} = 0.47 \mu\text{m}$ ) and the *r* band ( $\lambda_{\text{eff}} = 0.61 \mu\text{m}$ ) of SDSS9 (Ahn et al. 2012). For source No. 57, *g* and *r* band magnitudes are adopted from the SDSS7 catalogues (Abazajian et al. 2009) because the magnitudes of the source in SDSS9 seem contaminated by a neighbouring source. The values of  $\log_{10} \left( \frac{F_x}{F_{\text{opt}}} \right)$  of sources with SDSS9

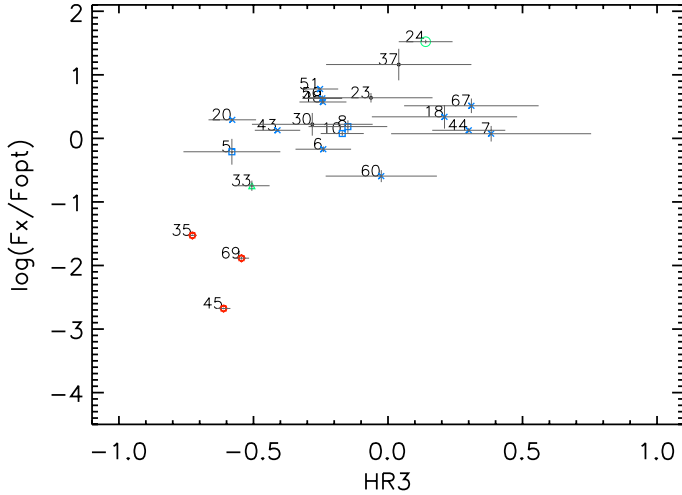


**Fig. 5.** X-ray to optical logarithmic ratio  $\log_{10}\left(\frac{F_x}{F_{\text{opt}}}\right)$  over hardness ratio  $HR_3$ . For the different source classes the same symbol types are used as in Fig. 2.

**Table 4.** *Chandra* flux of the sources that were also detected with *XMM-Newton*.

ID No.*	Flux (0.2–12.0 keV) [erg s <sup>-1</sup> cm <sup>-2</sup> ]	Confidence limits <sup>†</sup>	
		[erg s <sup>-1</sup> cm <sup>-2</sup> ]	[erg s <sup>-1</sup> cm <sup>-2</sup> ]
13	6.94e-15	1.10e-14	2.85e-15
20	9.20e-14	9.78e-14	8.70e-14
23	1.55e-14	1.77e-14	1.34e-14
29	3.37e-15	4.57e-15	2.18e-15
30	5.21e-15	6.49e-15	3.93e-15
33	3.64e-15	4.63e-15	2.64e-15
35	8.24e-13	8.39e-13	8.17e-13
38	6.08e-15	7.15e-15	5.03e-15
39	3.50e-15	4.11e-15	2.90e-15
40	7.39e-15	8.45e-15	6.31e-15
47	9.62e-15	1.22e-14	7.29e-15
48	4.57e-14	4.97e-14	4.17e-14
49	1.59e-14	1.80e-14	1.39e-14
51	9.78e-14	1.03e-13	9.37e-14
54	6.80e-15	8.45e-15	5.13e-15
56	7.44e-15	8.78e-15	6.14e-15
58	6.22e-15	8.22e-15	4.22e-15
67	2.38e-14	2.77e-14	1.99e-14
68	2.38e-14	3.84e-14	9.28e-15
70	–	–	2.90e-14

**Notes.** (\*) ID numbers are according to the *XMM-Newton* catalogue; (<sup>†</sup>) confidence limits for the flux are calculated according to [Evans et al. \(2010\)](#). Fluxes, upper, and lower limits have been converted to the *XMM-Newton* energy range.

counterparts are listed in Table A.2. Figure 5 shows a diagram with the  $\log_{10}\left(\frac{F_x}{F_{\text{opt}}}\right)$  and  $HR_3$  values (see Sect. 3.4).

### 3.3. Spectral analysis

We extracted the spectra of 27 sources for which we obtained  $\geq 300$  counts in the energy range of 0.2–12 keV in the EPIC data of one observation. All the other sources are too faint and do not have enough statistics for spectral analysis<sup>3</sup>. For many sources,

<sup>3</sup> The only bright source without spectral analysis is source No. 69. It was located at the position of a damaged pixel of the EPIC-pn in both observations (OBS4 and OBS5) in which this source was detected.

poor statistics did not allow us to find a significant model for the source spectra. We were able to fit 13 sources with the power-law, APEC, VAPEC, and MEKAL models by using XSPEC (ver.12.8.1). The PHABS model was used for the absorption. We fitted the spectra of the three EPIC detectors simultaneously for each source.

For the faintest sources that were detected on more than one EPIC image of the same observation, the significance of the fit parameters improves by combining the spectra of all EPICs using the task EPICscombine of SAS (V.13.5). It is reasonable to merge the spectra if the statistical error of the source is larger than the systematic error of the EPIC detectors<sup>4</sup>. Table 5 shows the results of the spectral analysis of the hard sources that were fit with the power-law model.

### 3.4. Hardness ratio

Hardness ratios can be used to study the spectral properties for fainter sources. The hardness ratio  $HR_i$  and its error  $EHR_i$  are defined as

$$HR_i = \frac{B_{i+1} - B_i}{B_{i+1} + B_i}; \quad EHR_i = 2 \frac{\sqrt{(B_{i+1}EB_i)^2 + (B_iEB_{i+1})^2}}{(B_{i+1} + B_i)^2}, \quad (5)$$

for  $i = 1, \dots, 4$ ;  $B_i$  is the count rate; and  $EB_i$  is the corresponding error in each energy band. For each source, we calculated the average of hardness ratios from the observation in which the source had the highest flux. Hardness ratios were calculated if the detection maximum likelihood of the source in each of the respective energy bands was higher than 6 ( $>3\sigma$ ). Figure 6 shows the hardness ratios of the sources with uncertainties  $< 0.3$ . In the same plot, we also overplotted the lines presenting the hardness ratios calculated using different spectral models with various column densities from  $N_H = 10^{20} \text{ cm}^{-2}$  to  $N_H = 10^{24} \text{ cm}^{-2}$ . We used absorbed power-law models with different photon-indexes  $\Gamma = 1, 2, 3$  corresponding to the X-ray binaries (XRBs) or AGNs. Two absorbed disk black-body models with temperatures  $kT_{\text{in}}$  of 0.5 keV and 1.0 keV were used for XRBs in soft state. Four thermal plasma models APEC with different temperatures  $kT_{\text{aptec}}$  of 0.2 keV, 0.5 keV, 1.0 keV, and 1.5 keV were used for supernova remnants, and two black-body models with temperatures of  $kT_{\text{bb}}$  of 50 eV and 100 eV for super-soft sources ([Ducci et al. 2013](#)).

## 4. Source classification

To classify the X-ray sources, we used the results of the analysis of the X-ray variability, the spectra, and the hardness ratios (see Sect. 3) as well as the results of the cross-correlation with sources in catalogues of different wavelengths (see Sect. 2.3). If a source satisfied the criteria of a specific class, it was classified as a candidate of that class.

### 4.1. Foreground stars

Depending on the effective temperature of a star, different mechanisms are responsible for its X-ray emission. Around massive stars like O, B, or Wolf-Rayet stars, shocks forming in the stellar wind create a plasma of a million degrees and produce X-ray emission. Cooler stars of the classes F to M can have

<sup>4</sup> [http://xmm.esac.esa.int/sas/current/documentation/threads/EPIC\\_merging.shtml](http://xmm.esac.esa.int/sas/current/documentation/threads/EPIC_merging.shtml)

**Table 5.** Spectral parameters of the hard sources in the field of the Draco dSph.

ID No.	OBS	EPIC*	$N_{\text{H}}(10^{22} \text{ cm}^{-2})$	$\Gamma$	Norm.	$\chi^2_{\nu}$ (d.o.f.)
6	2	PN	0.02*	$1.2^{+0.5}_{-0.3}$	$7.8^{+1.9}_{-1.9} \times 10^{-6}$	1.1 (4)
10	5	PN	0.02*	$1.0^{+0.4}_{-0.4}$	$1.2^{+0.6}_{-0.4} \times 10^{-5}$	0.4 (3)
12	2	Merged	0.02*	$0.9^{+0.2}_{-0.2}$	$6.5^{+1.7}_{-1.5} \times 10^{-6}$	1.4 (8)
14	5	PN	0.02*	$1.9^{+0.3}_{-0.3}$	$1.2^{+0.2}_{-0.2} \times 10^{-5}$	1.2 (6)
20	5	PN, MOS1, MOS2	0.02*	$2.4^{+0.1}_{-0.1}$	$2.7^{+0.2}_{-0.2} \times 10^{-5}$	0.9 (33)
24	1	Merged	0.02*	$0.7^{+0.2}_{-0.2}$	$4.7^{+1.5}_{-1.3} \times 10^{-6}$	0.8 (7)
33	4	PN, MOS1, MOS2	0.02*	$2.1^{+0.3}_{-0.2}$	$3.9^{+0.5}_{-0.5} \times 10^{-5}$	0.8 (12)
43	1	PN	0.02*	$2.4^{+0.1}_{-0.1}$	$1.7^{+0.1}_{-0.1} \times 10^{-4}$	0.8 (65)
48	2	Merged	0.02*	$1.1^{+0.2}_{-0.2}$	$5.2^{+1.1}_{-1.0} \times 10^{-6}$	1.7 (7)
50	5	PN	0.02*	$1.3^{+0.2}_{-0.2}$	$2.2^{+0.3}_{-0.3} \times 10^{-5}$	0.9 (11)
51	1	PN, MOS1, MOS2	0.02*	$1.9^{+0.1}_{-0.1}$	$2.7^{+0.2}_{-0.2} \times 10^{-5}$	0.7 (33)

**Notes.** (\*) PN, MOS1, and MOS2 are the EPIC detectors used for the simultaneous fits. “Merged” means that the three EPIC spectra were combined (see Sect. 3.3); (\*) parameter is frozen to the Galactic foreground  $N_{\text{H}}$  (Willingale et al. 2013).

magnetic coronae that are powered by flares due to reconnection in unstable magnetic fields (e.g. Güdel & Nazé 2009). Most of the late-type stars show variable X-ray emission. The ratio of X-ray to optical flux ( $\frac{F_{\text{x}}}{F_{\text{opt}}}$ ) varies from  $10^{-3}$  to  $10^{-7}$  for these stars. Massive stars show very low variability and their ratio of X-ray to optical flux is usually of the order of  $\frac{F_{\text{x}}}{F_{\text{opt}}} \sim 10^{-7}$  (Testa 2010). For the classification, we considered that stars are generally brighter in the optical than the X-ray regime ( $\frac{F_{\text{x}}}{F_{\text{opt}}} < 10^{-1}$ ) (e.g. Maccararo et al. 1988), and they are soft X-ray sources (see Table A.2 and Fig. 5).

In optical colour–colour and colour–magnitude diagrams, foreground stars can be distinguished from the stars in the Draco dSph (Fig. 2). In addition, we used the colour–magnitude diagrams in the near-infrared (2MASS survey) and infrared (WISE survey) to classify the foreground stars (Fig. 3).

Sources have been classified as foreground stars when the following conditions were satisfied:

$\log_{10}\left(\frac{F_{\text{x}}}{F_{\text{opt}}}\right) \leq -1$ ,  $HR_2 \leq 0.0$ ,  $HR_3 \leq -0.5$ ,  $HR_4 \leq -0.5$ ,  $g - r \leq 0.0$ ,  $g < 15.0$ ,  $J - K \leq 1.0$ ,  $K < 12.0$ , and  $W3 - W1 \leq 0.5$ . We classified source Nos. 16, 35, 39, 45, 59, and 69 as foreground stars. Except for source Nos. 35 and 45, these sources were previously classified as stars of the Draco dSph in MegaCam catalogue by Ségall et al. (2007). However, these bright sources have never been selected as members of the Draco dSph in other catalogues (see Sect. 2.3). As they fulfil all of our X-ray foreground star criteria, we consider them to be foreground stars. Spectral analysis has been performed for the brightest foreground stars, source Nos. 35 and 45:

**Source No. 35:** this source is the brightest X-ray source in the field of the Draco dSph. The source is an eclipsing binary of W UMa type (contact binary) and is named V\* GM Dra (Gazeas et al. 2005). We fitted its X-ray spectrum with two VAPEC models. VAPEC is the thermal plasma model APEC with variable abundances. Table 6 and Figure 7 show the details of the spectral analysis of this source which was performed using OBS1 data. The best fit was achieved when the carbon abundance was

**Table 6.** Fit parameters of source No. 35.

Model parameters	
$N_{\text{H}} (10^{22} \text{ cm}^{-2})$	$0.03^{+0.01}_{-0.01}$
$kT_1$ (keV)	$0.87^{+0.05}_{-0.06}$
Carbon	$0.24^{+0.03}_{-0.02}$
Norm.	$6.1^{+2.0}_{-1.6} \times 10^{-4}$
$kT_2$ (keV)	$0.51^{+0.09}_{-0.09}$
Norm.	$3.5^{+0.9}_{-0.7} \times 10^{-4}$
$\chi^2_{\nu}$ (d.o.f.)	1.07 (336)

**Notes.** Best-fit parameters of X-ray spectra of source No. 35 with the model PHABS  $\times$  (VAPEC + VAPEC). Errors are 90% confidence limits.

left free to vary. While the reduced  $\chi^2$  is 1.62 for 337 deg of freedom if the C abundance parameter is frozen to 1.0, it becomes 1.07 for 336 deg of freedom if C is freed (see Table 6). Therefore, the F-test probability that the two cases are consistent with each other is  $4.1 \times 10^{-32}$  and indicates that fitting the C abundance improves the fit significantly.

The average element-abundance in W UMa-type binaries usually is found to be lower than the solar photosphere value (e.g. Gondoin 2004b,a).

**Source No. 45:** we performed the spectral analysis for this source using the data of all the observations. Figure 8 and Table 7 show the fit model to this source in OBS2, which had the largest amount of counts for this source. The source is fitted well with a MEKAL model. Its place in the optical and infrared colour–colour diagrams as well as its X-ray-to-optical flux ratio is consistent with a foreground source (Figs. 2, 3, and 5). It is classified as a star in e.g. Röser et al. (2008) and Flesch (2010) and it is not reported as a variable source (e.g. Kinemuchi et al. 2008) or a binary system. Therefore, we classify this source as an isolated foreground star.

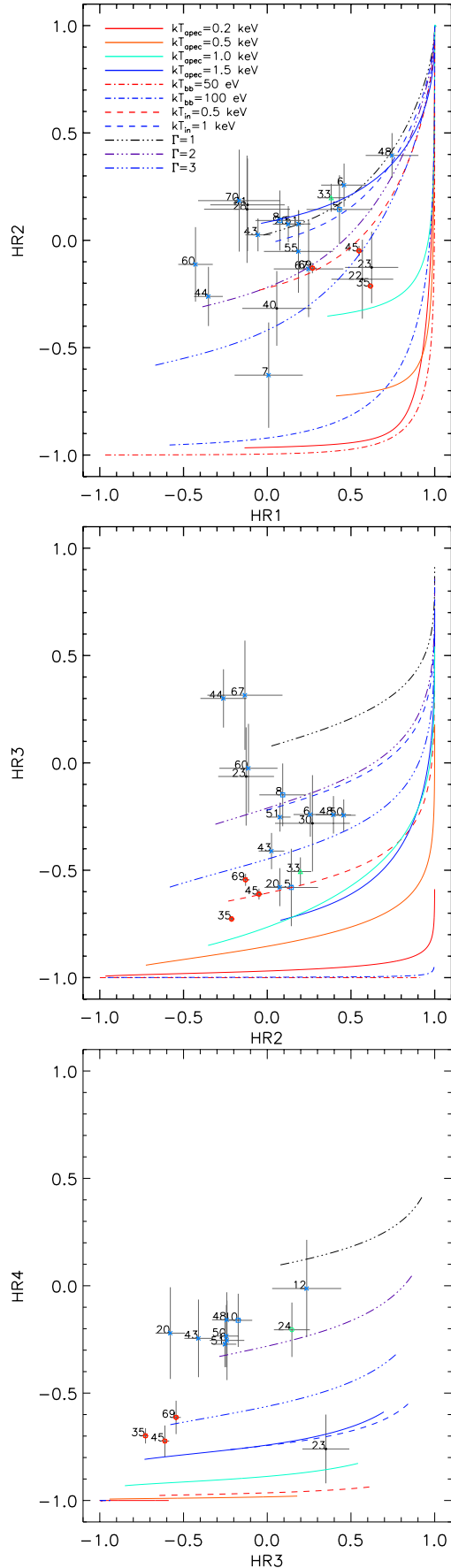


**Fig. 6.** Hardness ratio diagrams. The plotted lines are the hardness ratios calculated for different spectral models and column densities. For the different source classes the same symbol types are used as in Fig. 2.

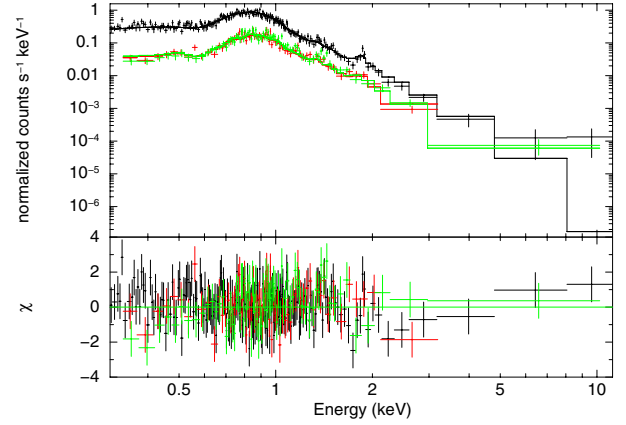


**Fig. 7.** EPIC counts spectra, together with residuals in units of standard deviations for source No. 35.

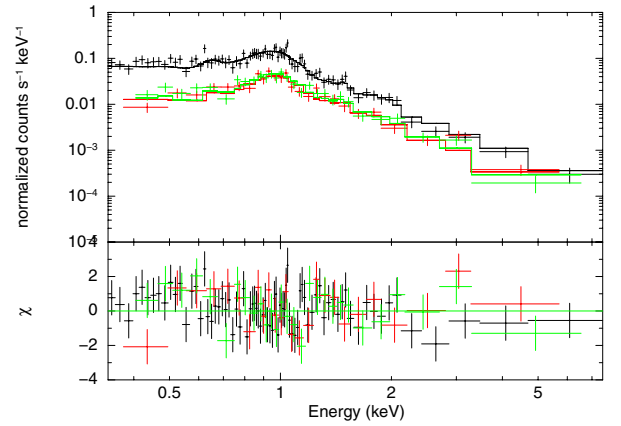


**Fig. 8.** EPIC counts spectra, together with residuals in units of standard deviations for source No. 45.

**Table 7.** Best-fit parameters of source No. 45.

Model parameters	
$N_{\text{H}}$ ( $10^{22}$ cm $^{-2}$ )	$0.00^{+0.01}$
$kT$ (keV)	$0.83^{+0.03}_{-0.04}$
Norm.	$5.8^{+0.7}_{-0.1} \times 10^{-5}$
$kT$ (keV)	$2.5^{+0.8}_{-0.2}$
Norm.	$1.6^{+0.8}_{-0.4} \times 10^{-4}$
$\chi^2_{\nu}$ (d.o.f.)	1.1 (127)

**Notes.** Best-fit parameters of X-ray spectra of source No. 45 with the model PHABS  $\times$  (MEKAL + MEKAL). Errors are 90% confidence limits.

## 4.2. Background objects

### 4.2.1. Active galactic nuclei

The majority of background objects are AGNs. With luminosities ranging from  $10^{42}$  to  $10^{48}$  erg s $^{-1}$ , they are the most luminous objects in the Universe, almost  $10^4$  times more luminous than normal galaxies (e.g. Jovanović & Popović 2009). One of the characteristics of AGNs is the fast variability which is observed in different parts of the electromagnetic spectrum. Fluctuations in the X-ray radiation on timescales from hours or minutes to several days are a common property of all AGNs (Krolik 1999).

**Table 8.** X-ray sources with counterparts in the 1.4 GHz NRAO VLA Sky Survey (NVSS-1998).

ID No.	NVSS-ID	Flux* (mJy)	Major axis (")	Minor axis (")
12	171919+575940	$8.7 \pm 0.5$	26.2	24.8
13	171920+575359	$3.5 \pm 0.4$	47.6	42.0
51	172051+575517	$57 \pm 2$	26.0	15.9

**Notes.** (\*) Integrated 1.4 GHz flux density of the radio source in mJy ( $10^{-26} \text{ W m}^{-2} \text{ Hz}^{-1}$ ).

The expected number of AGNs in the observed field can be calculated assuming the distribution of Cappelluti et al. (2009, see Eq. (8) in Sect. 5.1). Considering the area of the mosaic image in the energy band 0.2–5 keV, the total expected number of AGNs with fluxes  $\geq 1.7 \times 10^{-15} \text{ erg s}^{-1} \text{ cm}^{-2}$  is  $\sim 45$ . Therefore, more than half of the X-ray sources in the field of Draco are most likely AGNs.

Since there are catalogues in the literature based on a dedicated search for AGNs, we checked for correlations of the *XMM-Newton* sources with AGN catalogues (see Sect. 2.3). Source Nos. 6, 7, 20, 43, 44, 60, 68, and 70 have counterparts that were classified as AGNs, and the counterparts of source Nos. 18, 34, 36, 48, 50, 54, 55, and 67 were considered as AGN candidates in at least one of the AGN/quasar catalogues (see Sect. 2.3).

Pietsch et al. (2005) suggested that a harder X-ray source with  $HR_2 \geq -0.4$  with a radio counterpart is most likely a radio loud AGN. We found radio counterparts for source Nos. 12 and 51 in the catalogue of the 1.4 GHz NRAO VLA Sky Survey (NVSS-1998). Table 8 lists the details of the radio counterparts. Source No. 13 is a quasar for which the host galaxy has also been found (see Sect. 4.2.2). In addition to the  $HR_2$  criterion, sources identified as AGNs fulfil the following criteria:  $HR_3 \geq -0.5$  and  $HR_4 \geq -0.5$ .

All classified AGNs are point sources in the optical and infrared images and have the following properties:

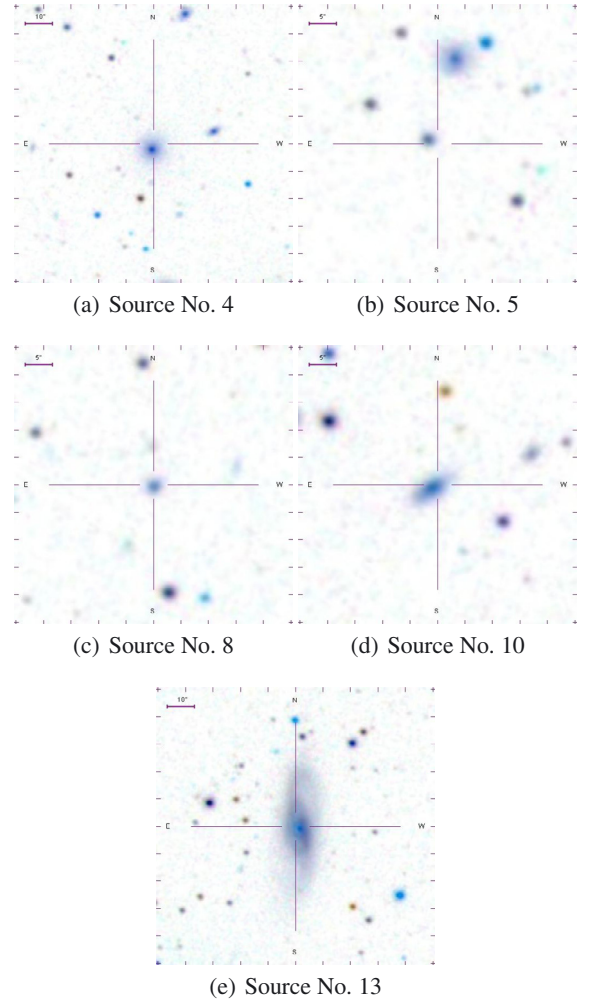
$$-1.0 \leq \log_{10}\left(\frac{F_x}{F_{\text{opt}}}\right) \leq 1.0, \quad -0.5 \leq g - r \leq 1.0, \quad \text{and} \\ -1.0 \leq g - i \leq 1.0.$$

The brightest classified AGN is source No. 43 with a total flux of  $6.66 \pm 2.84 \times 10^{-13} \text{ erg s}^{-1} \text{ cm}^{-2}$  in the energy range of 0.2–12 keV. For some of these AGNs, we performed a spectral analysis in which they are all fit well with a power-law model (Table 5).

#### 4.2.2. Galaxies

Since most galaxies are believed to host a black hole in their centre, the distinction between active and normal galaxies is difficult. It is assumed that in normal galaxies, the efficiency of the central super-massive black hole is low and the thermal emission from the centre is produced by bremsstrahlung (Bender 2005), while the main X-ray emission is caused by stars, accreting compact objects, supernova remnants, and soft diffuse emission (e.g. Trümper & Hasinger 2008).

We classified an X-ray source as a galaxy if its optical or infrared counterpart in the SDSS9 and WISE images is extended. Figure 9 shows the SDSS9 images of the galaxies (source Nos. 4, 5, 8, 10, and 13) which were classified by the star/galaxy classification catalogue (Vasconcellos et al. 2011) and the SDSS9 survey (Ahn et al. 2012). Source Nos. 41, 42, 53, and 66 were classified as galaxies in the SDSS7 and the SDSS9 survey

**Fig. 9.** SDSS9 images of galaxies in the field of the Draco dSph.

(Abazajian et al. 2009; Ahn et al. 2012). We considered these sources to be galaxy candidates. Source No. 13 (Fig. 9) is an optically dominant galaxy with a radio counterpart (see Table 8) which is classified as a quasar-galaxy (Bukhmastova 2001).

In colour–colour and colour–magnitude diagrams, the classified galaxies appear redder than AGNs in the optical wavelengths with  $g - i \gtrsim 1.0$  and  $g - r > 0.5$  (see Fig. 2). However, they do not show any noticeably special tendency in their X-ray luminosity or hardness ratios.

#### 4.3. Draco dSph sources

Since the Draco dSph galaxy is an old system we do not expect to detect X-ray sources associated with young stellar populations. Instead, we expect to find low-mass X-ray binaries (LMXBs), cataclysmic variables, or symbiotic stars.

##### 4.3.1. LMXB candidates

Low-mass X-ray binaries are binary systems that contain a neutron star or a black hole as a compact object and a low-mass companion like a red giant, a low-mass main sequence star ( $\lesssim 1 M_{\odot}$ ), or a white dwarf. The main part of the mass is usually transferred onto the compact object via an accretion disk yielding accretion rates of  $10^{-10} - 10^{-8} M_{\odot} \text{ yr}^{-1}$  (Tauris & van den Heuvel 2006). Population studies of the Galactic LMXBs show that

the majority of them have a luminosity of  $\sim 10^{35} - 10^{37}$  erg s $^{-1}$  (Fabbiano 2006). Persistent LMXBs with a red giant donor, which transfer matter to the compact object via Roche lobe overflow, have X-ray luminosities of  $\sim 10^{37}$  erg s $^{-1}$  (Zhu et al. 2012), while systems that transfer mass via stellar winds have a low X-ray luminosity of  $\sim 10^{33}$  erg s $^{-1}$ . In the case of transient LMXBs, the X-ray luminosity during quiescence is of the order of  $\sim 10^{32} - 10^{33}$  erg s $^{-1}$ . However, during outburst the X-ray luminosity can increase by several orders of magnitude, and the luminosity of the sources becomes comparable to that of persistent LMXBs. Some of the transient LMXBs show soft X-ray emission in quiescence which seems to depend on the accretion rate and the disk structure (Asai et al. 1998). In general, an LMXB can be characterised by a high ratio of X-ray to optical flux ( $\frac{F_x}{F_{opt}} \approx 10 - 10^4$ ), a faint blue optical counterpart, a lack of strong optical emission lines, and hard X-ray spectra (Schulz et al. 1989).

Sources No. 14, 24, and 64 showed hard spectra in both the spectral analysis and hardness ratios. Their optical counterparts were classified as stars in the Draco dSph by photometric methods (e.g. Piatek et al. 2001; Rave et al. 2003). Their X-ray-to-optical flux ratio is high, with  $\log_{10}(\frac{F_x}{F_{opt}}) \geq 1.0$  (Table A.2). They are probably X-ray binaries in the Draco dSph. Source No. 24 was classified as a candidate for a low redshift quasar by Abraham et al. (2012), who mainly characterised the nature of sources (quasars, galaxies, or stars) based on the colour–colour diagrams by using the SDSS7 data. The source is located in the region of quasars based on the colours of the SDSS7, but the  $u$  band magnitude of the SDSS9 survey is significantly different from that of SDSS7. With the colours of SDSS9 ( $u - g \approx 1.9$  and  $g - r \approx 0.7$ ), the source is located in the region of stars based on the colour–colour diagrams of Abraham et al. (2012). On the other hand, the optical counterpart is located far from classified AGNs in colour–magnitude diagram (Fig. 2). The source is not reported as an AGN in any other AGN catalogue. Therefore, we classified the source as a LMXB candidate.

Source No. 65: the source does not have an AGN counterpart in any other catalogues. We found a counterpart for the X-ray source in the optical MegaCam catalogue with magnitudes of  $g(0.47 \mu\text{m}) = (25.37 \pm 0.14)$  mag,  $r(0.62 \mu\text{m}) = (24.2 \pm 0.10)$  mag and  $i(0.81 \mu\text{m}) = (24.13 \pm 0.12)$  mag, and in the first look survey of the *Spitzer* Space Telescope (Fadda et al. 2004) with a magnitude of  $R = (24.4 \pm 0.15)$  mag. As indicated by the  $g - r$  colour index, the optical counterpart is a very faint red star. If this counterpart is associated with the X-ray source, the flux ratio of  $\log_{10}(\frac{F_x}{F_{opt}}) = 2.5$  indicates that the system is an LMXB in the Draco dSph. In addition, by applying the  $Z_n^2$  test for first and second harmonics, this source showed a high-significance pulsation at  $\sim 19.18$  s in the EPIC-pn data of OBS2 (see Sect. 3.1.1). The number of photons was 87. The probability that a peak is not caused by noise (but more likely by pulsation) was  $\sim 99.34\%$  ( $\geq 2.7\sigma$ ). For the number of independent trials we considered the number of searched harmonics ( $n = 1, 2$ ); the number of searched periods  $T_{exp}\Delta f$ , where  $T_{exp}$  is the exposure time and  $\Delta f \approx 6.8$  is the investigated frequency range (6.8 Hz is the Nyquist limit obtained from the time resolution of EPIC-pn in full-frame mode); and the number of detected sources in the random search for pulsation. The source was not detected in a 10 ks *Swift*/XRT (Burrows et al. 2005) observation carried out as two 5 ks observations in 2014. The  $3\sigma$  upper limit

of the 0.3–10 keV flux is  $4.1 \times 10^{-14}$  erg cm $^{-2}$  s $^{-1}$ . The source might be variable, having a flux during the *Swift* observations. The pulsation signal at  $\sim 19.18$  s must be taken with caution and it requires further investigation.

#### 4.3.2. Other binary systems

Interacting binaries consisting of a white dwarf accreting mass from a cool, late-type companion star are called cataclysmic variables and can be divided into different subtypes (Seward & Charles 2010). Cataclysmic variables in general show high variability because of the outbursts caused by accretion. Their luminosities range from  $10^{30} - 10^{34}$  erg s $^{-1}$  (Sazonov et al. 2006).

Source No. 27: its optical counterpart is a known symbiotic star in the Draco dSph, which has been called Draco C1 (Belczyński et al. 2000). Symbiotic stars are interacting binary systems of a late-type giant star and a compact companion (usually a white dwarf), which show far ultraviolet and soft X-ray emission. The source was studied in long-term optical photometry over years and shows a significantly variable light curve (e.g. Kinemuchi et al. 2008; Henden & Munari 2008). It was classified as a white dwarf in the Milky Way based on GALEX data (Bianchi et al. 2011). However, its high variability and luminosity are more consistent with a symbiotic system at the distance of the Draco dSph ( $\sim 93$  kpc, Munari & Buson 1994) than with a white dwarf in the Milky Way. In addition, the radial velocity of the source is comparable to that of the Draco dSph members ( $-311.7 \pm 13.5$ ; Margon et al. 2002). The relatively low  $\log_{10}(\frac{F_x}{F_{opt}}) = -1.51 \pm 0.10$  indicates that the optical emission dominates the X-ray emission. Since the source was not bright enough in any *XMM-Newton* observation, we could not study its X-ray spectrum or the hardness ratios.

Source No. 31: this source was classified as a member of the Draco dSph in different radial velocity measurements (e.g. Kleyna et al. 2002; Olszewski et al. 1995). The behaviour of the source in both the optical and infrared colour–magnitude diagrams is far from the typical foreground stars and seems more similar to source No. 27, which is a symbiotic star (see Figs. 2 and 3).

The infrared colours of the counterpart  $J - K \lesssim 0.9$  and  $I - J \lesssim 0.3$ , i.e. obtained from the infrared surveys 2MASS and the *William Herschel* Telescope, indicate that the source is located in the region of the red-giant branch of the Draco dSph, according to the classification of Cioni & Habing (2005). The source is likely a binary system in the Draco dSph, which contains at least one red giant, but the exact nature of the system is not clear.

Source No. 33: this source is the most variable source (Fig. 4) that has been found in this catalogue (variability factor  $Var = 49 \pm 12$ ). This high variability factor is related to the higher flux of the source in OBS4 compared to the other observations (see Appendix A). It seems that the source was detected during a flare or an outburst in OBS4. We fitted a power-law model to the spectrum of the source in OBS4 (Table 5). Figure 6 shows the hardness ratio of the source in OBS4 (the observation with the best statistics for this source), but the hardness ratio of the source in OBS1 and OBS2, i.e. before the increase of the flux, is much softer than in OBS4. It shows a very soft spectrum in OBS1, with  $HR_1 = 0.5 \pm 0.2$  and  $HR_2 = -0.8 \pm 0.2$ . The source was also detected by *Chandra* with a flux of  $(4.35 \pm 1.20) \times 10^{-15}$  erg s $^{-1}$  cm $^{-2}$  in the energy

range of 0.5–7.0 keV. Its hardness ratios of *Chandra* are not significant enough but show a soft behaviour (Evans et al. 2010). The flux ratio  $\log\left(\frac{F_x}{F_{\text{opt}}}\right) = -1.01 \pm 0.07$  indicates that this source is dominant in the optical. The optical and infrared colours and the variability are not consistent with a foreground star (see Figs. 2 and 3). These properties make it a possible candidate for a cataclysmic variable in the Draco dSph.

#### 4.4. Hard sources

We classified a source as a hard source when it has  $HR_2 - EHR_2 > -0.2$ , or only  $HR_3$  and/or  $HR_4$  are defined and there is no other classification (Pietsch et al. 2005). These sources can either be background AGNs or X-ray binaries in the Draco dSph. We classified source Nos. 21, 25, 28, 30, 37, 38, 47, 49, and 58 as hard sources.

## 5. Discussion

According to theoretical models, X-ray binary systems are supposed to form a few Gyr after the general star formation bursts in galaxies (e.g. White & Ghosh 1998). Since compact objects usually consume the mass of the donor star in a few hundred million years, any presence of LMXBs in dwarf galaxies with no star formation activity is challenging (Maccarone et al. 2005).

There are different explanations. One scenario is a dynamical interaction similar to the scenario in globular clusters, which leads to the late formation of new X-ray binaries (Hills 1976). Other scenarios for the presence of LMXBs in dwarf galaxies are accretion disks with very low duty cycles (Piro & Bildsten 2002) or ultra-compact objects (neutron stars or black holes) that formed through accretion onto a white dwarf (Bildsten & Deloye 2004).

### 5.1. X-ray luminosity function

In order to study the population of X-ray binaries in Draco dSph galaxy, we calculated the X-ray luminosity function (XLF) in the energy ranges of 0.5–2.0 keV and of 2.0–10 keV using data of all EPICs of five observations. In both energy bands, we considered all sources with  $ML > 10$  that were in the final catalogue. All sources classified as foreground stars or white dwarf binary systems (Sect. 4.3.2) were excluded. The count rate was converted to flux by using the ECF of Table 2. Since the sensitivity of the EPICs is not uniform across the FOV, the detection of the source in a given flux depends on its position in the FOV. Therefore, the effective area for the fainter sources is smaller than for the brightest sources, which are observable across the entire FOV of the EPICs. The underestimation of the number of sources observed at the faintest flux level affects the XLF such that it flattens at low luminosities. The incompleteness of XLFs is corrected by the sky-coverage function, which is the effective area as a function of flux. We created a sensitivity map of the mosaic image with the SAS task `esensmap`. For the creation of the sensitivity map, it is necessary to have exposure maps, background images for a specific energy range, and a detection mask, which are all produced using the SAS task `emosaicproc` for each observation in the process of source detection for the mosaic image. The mosaic sensitivity map was created using the merged exposure maps and background images. Figure 10 shows the sky coverage function of the mosaic sensitivity map in two different energy bands. The cumulative XLF is corrected for incompleteness by

$$N(>F_x) = A_{\text{tot}} \sum_{i=1}^{N_s} \frac{1}{\omega(F_i)}, \quad (6)$$

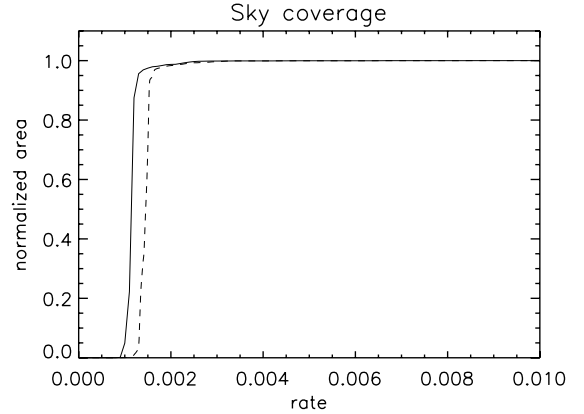


**Fig. 10.** Sky coverage of the mosaic sensitivity map as a function of the X-ray count rate (2–10 keV, dashed line) and (0.5–2 keV, solid line).

where  $N(>F_x)$  is the number of sources with a flux higher than  $F_x$ . For each source with a flux  $F_i$ , the number is weighted by the normalised effective area  $A_{\text{tot}}/\omega(F_i)$ , where  $A_{\text{tot}}$  is the total area observed by the EPICs,  $\omega(F_i)$  is the sky-coverage function and  $N_s$  is the total number of detected sources. Every source is hence weighted and the XLF corrected for incompleteness. The variance of the source number counts is calculated by

$$\sigma^2 = \sum_{i=1}^{N_s} \left( \frac{A_{\text{tot}}}{\omega(F_i)} \right)^2. \quad (7)$$

The XLF obtained by the method described above consists of X-ray sources belonging to the Draco dSph and background AGNs. We eliminated the AGN contribution by using the AGN XLF of the XMM-COSMOS survey (Cappelluti et al. 2009). They calculated the  $\log N - \log S$  of AGNs in two energy bands, 0.5–2.0 keV and 2.0–10 keV, which allows us to subtract the AGN  $\log N - \log S$  from the distribution of X-ray sources of a galaxy. The XLF of AGNs is described by a broken power-law,

$$\frac{dN}{dF} = \begin{cases} AF^{-\alpha_1} & F > F_b \\ BF^{-\alpha_2} & F \leq F_b, \end{cases} \quad (8)$$

where  $A = BF_b^{\alpha_1 - \alpha_2}$  is the normalisation. In the 2.0–10 keV, the best-fit parameters are  $\alpha_1 = 2.46 \pm 0.08$ ,  $\alpha_2 = 1.55 \pm 0.18$ ,  $F_b = (1.05 \pm 0.16) \times 10^{-14} \text{ erg cm}^{-2} \text{ s}^{-1}$ , and  $A = 413$ . In the 0.5–2 keV energy band the parameters are  $\alpha_1 = 2.40 \pm 0.05$ ,  $\alpha_2 = 1.60^{+0.04}_{-0.10}$ ,  $F_b = 1.00^{+0.21}_{-0.26} \times 10^{-14} \text{ erg cm}^{-2} \text{ s}^{-1}$ , and  $A = 141$ . We used the absorbing column density of  $N_H = 2.46 \times 10^{20} \text{ cm}^{-2}$  (Willingale et al. 2013). Figure 11 shows the XLFs of the X-ray sources in the 2.0–10 keV and the 0.5–2 keV energy band for OBS 1, 2, 3, and 5. The XLF in the energy band of 2.0–10 keV shows high contamination by AGNs.

We also calculated the XLF in the 0.5–2 keV. In this energy range we had many more sources with  $ML > 10$ . The 0.2–5 keV XLF in Fig. 11 shows an excess in the number of sources (compared to the AGN distribution) in the luminosity range between  $\sim(1.4-3) \times 10^{33} \text{ erg s}^{-1}$  (assuming  $D = 82.4 \text{ kpc}$ ) of  $\sim 10$ . These sources can be either accreting white dwarfs or transient LMXBs observed during low luminosity states. Binary systems that have a white dwarf as a compact object with typical accretion rates of  $10^{-12} - 10^{-9} M_\odot \text{ yr}^{-1}$  can have X-ray luminosities of  $10^{31} - 10^{34} \text{ erg s}^{-1}$ . Transient LMXBs during low luminosity states can also have X-ray luminosities in the range of  $10^{32} - 10^{33} \text{ erg s}^{-1}$  (see Sect. 4.3.1).

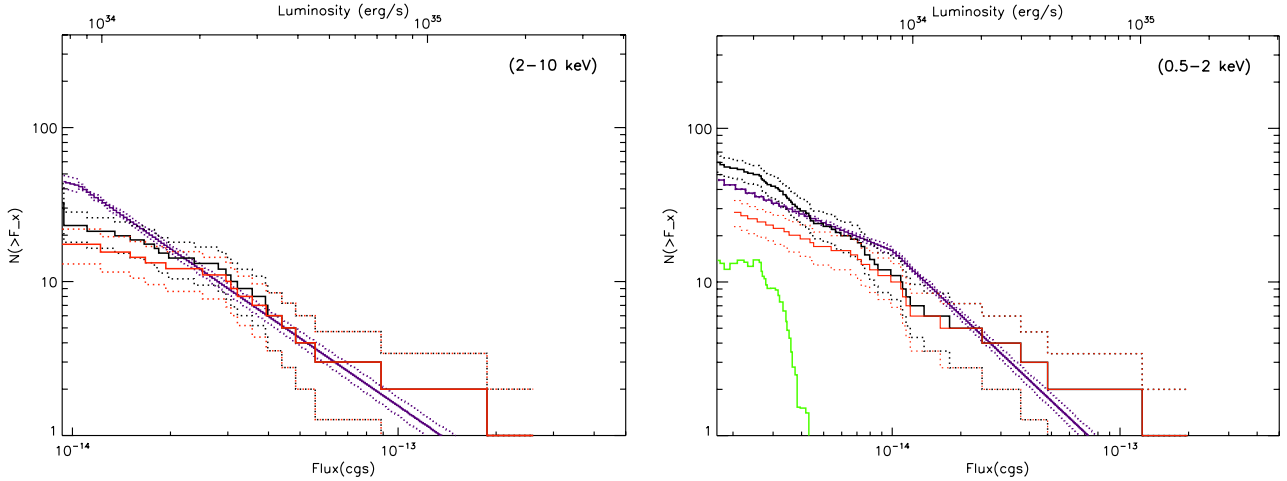


**Fig. 11.** Cumulative XLFs corrected for incompleteness, in the 2–10 keV (left panel) and 0.5–2 keV (right panel) energy bands. Black lines correspond to the XLFs without foreground stars, symbiotic systems, and binary candidates as classified in Sect. 4.3.2, corrected for incompleteness. Red lines show the XLFs of the classified AGNs. Blue lines are the AGN XLFs of Cappelluti et al. (2009). Green lines show the XLFs of X-ray sources after subtracting the contribution of the AGNs (blue lines) from X-ray sources in the dwarf galaxy (black lines). The dashed lines are the 90% confidence errors.

To make a more significant estimation of the expected number of XRBs in this dwarf galaxy more observations are necessary.

### 5.2. Dark matter halo and LMXBs

Based on the *XMM-Newton* study of the Sculptor dSph, Maccarone et al. (2005) reported that the optical counterparts of five X-ray sources have colours and magnitudes consistent either with giant branch stars or with horizontal branch stars in the Sculptor dSph, and all have proper motion estimates that indicate a probability of at least 96% that these sources are members of the Sculptor dSph. Therefore, these five sources were classified as LMXBs located in Sculptor dSph. However, more updated observations have shown that two of them are AGNs<sup>5</sup>.

Detections of LMXBs in the Sculptor dSph (Maccarone et al. 2005) and now in the Draco dSph would mean that they have retained their X-ray binaries. Dehnen & King (2006) raised the question of how the X-ray binaries can be retained by the host dwarf galaxy in spite of their high proper motion. They concluded that the most likely explanation for the presence of LMXBs in Sculptor dSph galaxy would be a dark matter halo with a mass of the order of  $\geq 10^9 M_{\odot}$ . The run-away speeds of X-ray binary systems caused by an asymmetry in supernova explosions were calculated in several works (e.g. Brandt & Podsiadlowski 1995). These studies show that LMXBs have a mean kick velocity of  $\sim 200 \text{ km s}^{-1}$  (Brandt & Podsiadlowski 1995; Zhang et al. 2013).

In the case of the Sculptor galaxy, Dehnen & King (2006) estimated a minimum required mass of the dark matter halo to hold the LMXBs with velocities between  $20\text{--}60 \text{ km s}^{-1}$  by assuming a pseudo-isothermal sphere model with a radius of 1.5 kpc for the galaxy, a mass of  $5 \times 10^7 M_{\odot}$ , and a truncation radius that exceeds 15 kpc. They selected different radii for the dark matter halo core to show how massive the total mass

should be to keep the LMXBs in the potential. According to this model, a dark matter core with a radius of  $\sim 3\text{--}5 \text{ kpc}$  is needed to hold the LMXBs in the Sculptor dSph with a speed between  $40\text{--}60 \text{ km s}^{-1}$ . It also implies that the total mass of the galaxy should be of the order of  $10^{10} M_{\odot}$ , which is more massive than other estimates ( $\sim 10^8 M_{\odot}$ ; e.g. Battaglia et al. 2008; Amorisco et al. 2014).

The total *i*-band brightness of the Draco dSph is  $L/L_{\odot} = (2.4 \pm 0.5) \times 10^5$  (Odenkirchen et al. 2001). Under the assumption of Virial equilibrium, the high stellar velocity dispersion implies an extremely high mass to light ratio, of about  $146 \pm 42 (M/L)_{\odot}$  (Odenkirchen et al. 2001),  $330 \pm 125 (M/L)_{\odot}$  (Kleyna et al. 2002),  $\sim 416 (M/L)_{\odot}$  (e.g. Ségall et al. 2007; Read et al. 2006), and even up to  $440 (M/L)_{\odot}$  (Faria et al. 2007). Draco dSph is believed to be a flawless dwarf galaxy, i.e. it is not a remnant of a tidally disrupted satellite galaxy, as both observational studies and simulations have shown (Łokas 2002; Klessen et al. 2003; Read et al. 2006; Mashchenko et al. 2006; Ségall et al. 2007). Instead, it is most likely strongly dark matter dominated. Based on this background we try to understand how consistent the estimated mass of the dark matter halo is with the mass required to retain the LMXBs.

The most recent optical observations of Draco dSph suggest a visible galaxy core of  $7.7'$  (corresponding to 0.18 kpc at a distance of 82 kpc, Kinemuchi et al. 2008), and a stellar truncation radius of  $\sim 40.1'$  (corresponding to 0.96 kpc, Odenkirchen et al. 2001). The velocity dispersion of the Draco dSph measured in many observations is between  $9\text{--}11 \text{ km s}^{-1}$ . Kleyna et al. (2001) found the first evidence of an extended dark matter halo in the Draco dSph. They showed that the velocity dispersion with two different dark matter halo models consistently implies a mass of  $M = 8_{-2}^{+3} \times 10^7 M_{\odot}$  inside a dark matter halo core of  $r_c = 29'$ . Consistent with this result, a sharp decline in the velocity dispersion outside  $\sim 30'$  was reported by Wilkinson et al. (2004). On the basis of this new data of Wilkinson et al. (2004), Łokas et al. (2005) performed another study of the Draco dSph dark matter distribution and calculated a mass of  $M = 6.6 \times 10^7 M_{\odot}$  which is lower than the estimated mass by Kleyna et al. (2001). On the other hand, *N*-body simulations of Read et al. (2006) in different initial conditions were fitted to observational data of

<sup>5</sup> The source at RA = 01h00m26.19s, Dec =  $-33^{\circ}41'07''.5$  (J2000) has a quasar as its counterpart with a redshift of  $z = 0.60$  at a distance of  $\sim 0.5'$  (Véron-Cetty & Véron 2010a; Souchay et al. 2012), and the source at RA = 00h59m52.75s, Dec =  $-33^{\circ}44'26''.1$  (J2000) has a quasar candidate with  $z = 0.07$  at a distance of  $\sim 1''$  (Flesch 2010; Jones et al. 2009) as its counterpart.

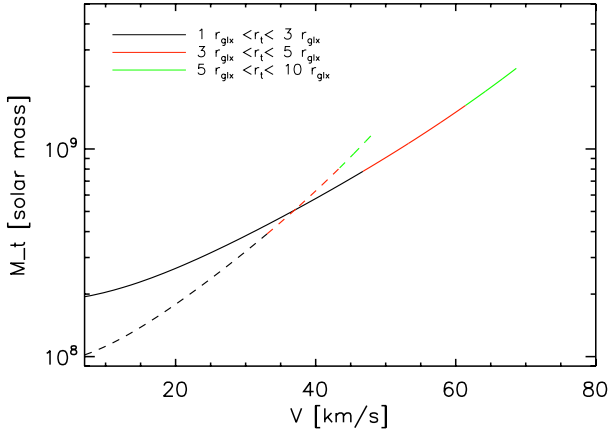


**Fig. 12.** Minimum mass of the extended dark matter halo of the Draco dSph, which is needed to hold a LMXB with the velocity  $V$  at the radius 1 kpc. The halo core radius is 0.70 kpc and the assumed mass is  $M = 5 \times 10^7 M_\odot$  (dashed line) or  $8 \times 10^8 M_\odot$  (solid line) within 0.96 kpc. The truncation radius changes with colours. Black, red, and green correspond to 3, 5, and 10 times the visible radius of the galaxy.

Wilkinson et al. (2004) and suggest a mass of  $\sim 10^8 M_\odot$  inside 0.8 kpc for the Draco dSph (Model D in the paper).

Considering the above results and following the method by Dehnen & King (2006), we calculate the total mass in the Draco dSph necessary to keep the LMXBs with the speed  $V$ . The model for halo follows the formula

$$GM(<1) = V_0^2 \frac{r^3}{r^2 + r_c^2}. \quad (9)$$

By assuming a dark matter core radius of  $r_c = 29'$  (0.70 kpc at the distance of 82 kpc, Kinemuchi et al. 2008), and a radius of the galaxy of  $r = 40'$  (0.96 kpc at the distance of 82 kpc), the circular velocity is

$$V_0 = \sqrt{\frac{GM}{0.96 \text{ kpc}}} \times \sqrt{1 + \left(\frac{0.70}{0.96}\right)^2}. \quad (10)$$

With  $r_t$  being the truncation radius of the galaxy, the velocity  $v_{\text{esc}}$  at radius  $r < r_t$  required to escape outside  $r_t$  is

$$V_{\text{esc}}^2 = V_0^2 \ln \left( \frac{r_t^2 + r_c^2}{r^2 + r_c^2} \right). \quad (11)$$

Inside the visible galaxy, we assumed two different dark masses of  $M_{\text{min}} = 5 \times 10^7 M_\odot$  and  $M_{\text{max}} = 10^8 M_\odot$ . We calculated the halo mass required to keep an LMXB moving out with the velocity  $v$  from  $r = 1$  kpc, which is already larger than the radius of the galaxy. The truncation radius of the halo can vary between 3–10 times the stellar radius (e.g. Duc et al. 2004; Bournaud et al. 2003). However, we note that large halo truncation radii (approximately 10 times the galaxy radius) are suggested in tidal dwarf galaxy models (e.g. Bournaud et al. 2003; Duc et al. 2004). Without any tidal effect, it seems unlikely that the Draco dSph extends up to 10 times the visible radius. In Fig. 12, we show how the amount of the mass changes by assuming a dark matter truncation radius of 3–10 times the galaxy radius. Different colours present different ranges of the truncation radius from minimum to maximum.

The circular velocity calculated by Eq. (10) is between  $\sim 27$ – $38 \text{ km s}^{-1}$ . The amount of the circular velocity plays an important role in the estimation of both total mass and the escape velocity in this model. Our estimation is consistent with

the result of Kazantzidis et al. (2004), who have shown that by using an isotropic and a tangentially anisotropic model, a maximum circular velocity of  $\sim 20$ – $35 \text{ km s}^{-1}$  fits the data well.

As shown in Fig. 12, even assuming the highest total mass inside the visible radius of the Draco dSph and extending the truncation radius of the dark matter halo to 10 times the visible radius, the galaxy is only able to keep LMXBs with speeds lower than  $\sim 70 \text{ km s}^{-1}$ , which is lower than the mean speed of  $200 \text{ km s}^{-1}$  of the majority of the LMXBs (Zhang et al. 2013). However, we do not know the accurate distribution of the runaway speed of LMXBs, or the mass or truncation radius of the galaxy. We will need a better estimate of the number of LMXBs in the dSphs to have a clearer value of the required total mass of such galaxies.

## 6. Summary

We present the X-ray analysis of five *XMM-Newton* observations of the Draco dSph. We performed source detection separately for each image in each observation and for the total band mosaic image and produced a catalogue of 70 X-ray sources. The sources were classified through cross-correlation with other catalogues, spectral analysis, hardness ratio diagrams, and variability studies. We classified 18 sources as AGNs and 9 sources as galaxies and galaxy candidates. Six sources were classified as foreground stars and one source as a foreground contact binary system in the Milky Way. Four sources were classified as LMXB candidates. One of them shows a significant pulsation, while the others were classified based on the X-ray-to-optical flux ratio and their position in the colour–magnitude diagram. We also found a symbiotic star, a candidate of cataclysmic variable, and a binary system in the Draco dSph. Based on hardness ratios we classified 9 hard sources, which can be AGNs or LMXBs, in the field of the Draco dSph.

We derived the XLFs of the X-ray sources in the energy ranges of 2.0–10 keV and 0.5–2 keV. The XLFs indicate that X-ray sources in the field of the Draco dSph are strongly contaminated by AGNs. The 0.2–5 keV XLF shows an excess of sources (compared to the AGN distribution) in the flux range of  $\sim 1.7 \times 10^{-15}$ – $4.5 \times 10^{-15} \text{ erg s}^{-1} \text{ cm}^{-2}$  of about ten, which are most likely objects in Draco dSph. For a better study of the LMXB population, longer observations are necessary.

On the basis of the consideration of the escape velocity of the LMXBs, we estimated the required dark matter halo mass to keep the LMXBs in the Draco dSph. Our calculation shows that the Draco dSph seems not to be able to retain its LMXBs; however, this result requires further investigation owing to the low photon statistics of the available data.

*Acknowledgements.* This research was funded by the Deutsche Forschungsgemeinschaft, through the Emmy Noether Research Grant SA 2131/1-1. L.D. acknowledges support by the Bundesministerium für Wirtschaft und Technologie and the Deutsches Zentrum für Luft und Raumfahrt through the grant 50 OG 1301. Based on observations obtained with *XMM-Newton*, an ESA science mission with instruments and contributions directly funded by ESA Member States and NASA. This research has made use of the SIMBAD and VIZIER database, operated at CDS, Strasbourg, France, and of the NASA/IPAC Extragalactic Database (NED), which is operated by the Jet Propulsion Laboratory, California Institute of Technology, under contract with the National Aeronautics and Space Administration. This publication makes use of data products from the Wide-field Infrared Survey Explorer, which is a joint project of the University of California, Los Angeles, and the Jet Propulsion Laboratory/California Institute of Technology, funded by the National Aeronautics and Space Administration. This publication has made use of data products from the Two Micron All Sky Survey, which is a joint project of the University of Massachusetts and the Infrared Processing and Analysis Center, funded by the National Aeronautics and Space Administration

and the National Science Foundation. Funding for SDSS and SDSS-III has been provided by the Alfred P. Sloan Foundation, the Participating Institutions, the National Science Foundation, and the U.S. Department of Energy Office of Science. The SDSS-III web site is <http://www.sdss3.org/>. SDSS-III is managed by the Astrophysical Research Consortium for the Participating Institutions of the SDSS-III Collaboration including the University of Arizona, the Brazilian Participation Group, Brookhaven National Laboratory, University of Cambridge, University of Florida, the French Participation Group, the German Participation Group, the Instituto de Astrofísica de Canarias, the Michigan State/Notre Dame/JINA Participation Group, Johns Hopkins University, Lawrence Berkeley National Laboratory, Max Planck Institute for Astrophysics, New Mexico State University, New York University, Ohio State University, Pennsylvania State University, University of Portsmouth, Princeton University, the Spanish Participation Group, University of Tokyo, University of Utah, Vanderbilt University, University of Virginia, University of Washington, and Yale University. This research has made use of data obtained from the *Chandra* Source Catalogue, provided by the *Chandra* X-ray Centre (CXC) as part of the *Chandra* Data Archive. This research has made use of SAOImage DS9, developed by Smithsonian Astrophysical Observatory. The National Radio Astronomy Observatory is a facility of the National Science Foundation operated under cooperative agreement by Associated Universities, Inc.

## References

- Abazajian, K. N., Adelman-McCarthy, J. K., Agüeros, M. A., et al. 2009, *ApJS*, **182**, 543
- Abraham, S., Philip, N. S., Kembhavi, A., Wadadekar, Y. G., & Sinha, R. 2012, *MNRAS*, **419**, 80
- Ahn, C. P., Alexandroff, R., Allende Prieto, C., et al. 2012, *ApJS*, **203**, 21
- Amorisco, N. C., Zavala, J., & de Boer, T. J. L. 2014, *ApJ*, **782**, L39
- Aparicio, A., Carrera, R., & Martínez-Delgado, D. 2001, *AJ*, **122**, 2524
- Asai, K., Dotani, T., Hoshi, R., et al. 1998, *PASJ*, **50**, 611
- Battaglia, G., Helmi, A., Tolstoy, E., et al. 2008, *ApJ*, **681**, L13
- Belczyński, K., Mikolajewska, J., Munari, U., Ivison, R. J., & Friedjung, M. 2000, *A&AS*, **146**, 407
- Bellazzini, M., Ferraro, F. R., Origlia, L., et al. 2002, *AJ*, **124**, 3222
- Bender, R. 2005, in *Growing Black Holes: Accretion in a Cosmological Context*, eds. A. Merloni, S. Nayakshin, & R. A. Sunyaev, 147
- Bianchi, L., Efremova, B., Herald, J., et al. 2011, *MNRAS*, **411**, 2770
- Bildsten, L., & Deloye, C. J. 2004, *ApJ*, **607**, L119
- Bournaud, F., Duc, P.-A., & Masset, F. 2003, *A&A*, **411**, L469
- Boyarsky, A., Ruchayskiy, O., Iakubovskiy, D., & Franse, J. 2014, *Phys. Rev. Lett.*, **113**, 251301
- Brandt, N., & Podsiadlowski, P. 1995, *MNRAS*, **274**, 461
- Buccheri, R., Bennett, K., Bignami, G. F., et al. 1983, *A&A*, **128**, 245
- Buccheri, R., Maccarone, M. C., Sacco, B., & di Gesù, V. 1988, *A&A*, **201**, 194
- Bukhmastova, Y. L. 2001, *Astron. Rep.*, **45**, 581
- Bulbul, E., Markevitch, M., Foster, A., et al. 2014, *ApJ*, **789**, 13
- Burrows, D. N., Hill, J. E., Nousek, J. A., et al. 2005, *Space Sci. Rev.*, **120**, 165
- Caffau, E., Ludwig, H.-G., Bonifacio, P., et al. 2010, *A&A*, **514**, A92
- Cappelluti, N., Brusa, M., Hasinger, G., et al. 2009, *A&A*, **497**, 635
- Cioni, M.-R. L., & Habing, H. J. 2005, *A&A*, **442**, 165
- Condon, J. J., Cotton, W. D., Greisen, E. W., et al. 1998, *AJ*, **115**, 1693
- Cutri, R. M., Skrutskie, M. F., van Dyk, S., et al. 2003, *VizieR Online Data Catalog: II/246*
- Cutri, R. M., Wright, E. L., Conrow, T., et al. 2012, *VizieR Online Data Catalog: II/311*
- D'Abrusco, R., Longo, G., & Walton, N. A. 2009, *MNRAS*, **396**, 223
- Dehnen, W., & King, A. 2006, *MNRAS*, **367**, L29
- Duc, P.-A., Bournaud, F., & Masset, F. 2004, *A&A*, **427**, 803
- Ducci, L., Sasaki, M., Haberl, F., & Pietsch, W. 2013, *A&A*, **553**, A7
- Evans, I. N., Primini, F. A., Glotfelty, K. J., et al. 2010, *ApJS*, **189**, 37
- Fabbiano, G. 2006, *ARA&A*, **44**, 323
- Fadda, D., Jannuzi, B. T., Ford, A., & Storrie-Lombardi, L. J. 2004, *AJ*, **128**, 1
- Falco, E. E., Kurtz, M. J., Geller, M. J., et al. 1999, *PASP*, **111**, 438
- Faria, D., Feltzing, S., Lundström, I., et al. 2007, *A&A*, **465**, 357
- Flesch, E. 2010, *PASA*, **27**, 283
- Gazeas, K. D., Baran, A., Niarchos, P., et al. 2005, *Acta Astron.*, **55**, 123
- Gibson, R. R., & Brandt, W. N. 2012, *ApJ*, **746**, 54
- Girardi, L., Grebel, E. K., Odenkirchen, M., & Chiosi, C. 2004, *A&A*, **422**, 205
- Gondoin, P. 2004a, *A&A*, **426**, 1035
- Gondoin, P. 2004b, *A&A*, **415**, 1113
- Güdel, M., & Nazé, Y. 2009, *A&ARv*, **17**, 309
- Henden, A., & Munari, U. 2008, *Baltic Astron.*, **17**, 293
- Hills, J. G. 1976, *MNRAS*, **175**, 1P
- Irwin, M., & Hatzidimitriou, D. 1995, *MNRAS*, **277**, 1354
- Jansen, F., Lumb, D., Altieri, B., et al. 2001, *A&A*, **365**, L1
- Jones, D. H., Read, M. A., Saunders, W., et al. 2009, *MNRAS*, **399**, 683
- Jovanović, P., & Popović, L. Č. 2009, ArXiv e-prints [[arXiv:0903.0978](https://arxiv.org/abs/0903.0978)]
- Kazantzidis, S., Mayer, L., Mastroiello, C., et al. 2004, *ApJ*, **608**, 663
- Kinemuchi, K., Harris, H. C., Smith, H. A., et al. 2008, *AJ*, **136**, 1921
- King, I. 1962, *AJ*, **67**, 471
- Klessen, R. S., Grebel, E. K., & Harbeck, D. 2003, *ApJ*, **589**, 798
- Kleyna, J. T., Wilkinson, M. I., Evans, N. W., & Gilmore, G. 2001, *ApJ*, **563**, L115
- Kleyna, J., Wilkinson, M. I., Evans, N. W., Gilmore, G., & Frayn, C. 2002, *MNRAS*, **330**, 792
- Kormendy, J. 1985, *ApJ*, **295**, 73
- Krolik, J. H. 1999, *Active galactic nuclei: from the central black hole to the galactic environment* (Princeton: Princeton University Press)
- Łokas, E. L. 2002, *MNRAS*, **333**, 697
- Łokas, E. L., Mamon, G. A., & Prada, F. 2005, *MNRAS*, **363**, 918
- Lovell, M. R., Bertone, G., Boyarsky, A., Jenkins, A., & Ruchayskiy, O. 2015, *MNRAS*, **451**, 1573
- Maccarone, T., Gioia, I. M., Wolter, A., Zamorani, G., & Stocke, J. T. 1988, *ApJ*, **326**, 680
- Maccarone, T. J., Kundu, A., Zepf, S. E., Piro, A. L., & Bildsten, L. 2005, *MNRAS*, **364**, L61
- Malyshev, D., Neronov, A., & Eckert, D. 2014, *Phys. Rev. D*, **90**, 103506
- Margon, B., Anderson, S. F., Harris, H. C., et al. 2002, *AJ*, **124**, 1651
- Mashchenko, S., Sills, A., & Couchman, H. M. 2006, *ApJ*, **640**, 252
- Metz, M., & Kroupa, P. 2007, *MNRAS*, **376**, 387
- Munari, U., & Buson, L. M. 1994, *A&A*, **287**, 87
- Nucita, A. A., Manni, L., De Paolis, F., Vetrugno, D., & Ingrosso, G. 2013, *A&A*, **550**, A18
- Odenkirchen, M., Grebel, E. K., Harbeck, D., et al. 2001, *AJ*, **122**, 2538
- Olszewski, E. W., Aaronson, M., & Hill, J. M. 1995, *AJ*, **110**, 2120
- Piatek, S., Pryor, C., Armandroff, T. E., & Olszewski, E. W. 2001, *AJ*, **121**, 841
- Pietsch, W., Freyberg, M., & Haberl, F. 2005, *A&A*, **434**, 483
- Piro, A. L., & Bildsten, L. 2002, *ApJ*, **571**, L103
- Rave, H. A., Zhao, C., Newberg, H. J., et al. 2003, *ApJS*, **145**, 245
- Read, J. I., Wilkinson, M. I., Evans, N. W., Gilmore, G., & Kleyna, J. T. 2006, *MNRAS*, **367**, 387
- Richards, G. T., Myers, A. D., Gray, A. G., et al. 2009, *ApJS*, **180**, 67
- Riemer-Sørensen, S., & Hansen, S. H. 2009, *A&A*, **500**, L37
- Röser, S., Schilbach, E., Schwan, H., et al. 2008, *A&A*, **488**, 401
- Rutledge, R. E., Brunner, R. J., Prince, T. A., & Lonsdale, C. 2000, *ApJS*, **131**, 335
- Saxton, R. D., Read, A. M., Esquej, P., et al. 2008, *A&A*, **480**, 611
- Sazonov, S., Revnivtsev, M., Gilfanov, M., Churazov, E., & Sunyaev, R. 2006, *A&A*, **450**, 117
- Scargle, J. D. 1982, *ApJ*, **263**, 835
- Schlafly, E. F., & Finkbeiner, D. P. 2011, *ApJ*, **737**, 103
- Schulz, N. S., Hasinger, G., & Truemper, J. 1989, *A&A*, **225**, 48
- Sérgall, M., Ibata, R. A., Irwin, M. J., Martin, N. F., & Chapman, S. 2007, *MNRAS*, **375**, 831
- Seward, F. D., & Charles, P. A. 2010, *Exploring the X-ray Universe* (Cambridge University Press)
- Souchay, J., Andrei, A. H., Barache, C., et al. 2012, *A&A*, **537**, A99
- Strüder, L., Briel, U., Dennerl, K., et al. 2001, *A&A*, **365**, L18
- Suchkov, A. A., Hanisch, R. J., Voges, W., & Heckman, T. M. 2006, *AJ*, **132**, 1475
- Tauris, T. M., & van den Heuvel, E. P. J. 2006, in *Formation and evolution of compact stellar X-ray sources*, eds. W. H. G. Lewin, & M. van der Klis, 623
- Testa, P. 2010, *Proc. National Academy of Science*, **107**, 7158
- Trümper, J. E., & Hasinger, G. 2008, *The Universe in X-Rays* (Berlin, Heidelberg: Springer)
- Turner, M. J. L., Abbey, A., Arnaud, M., et al. 2001, *A&A*, **365**, L27
- Vasconcellos, E. C., de Carvalho, R. R., Gal, R. R., et al. 2011, *AJ*, **141**, 189
- Véron-Cetty, M.-P., & Véron, P. 2010a, *A&A*, **518**, A10
- Véron-Cetty, M. P., & Véron, P. 2010b, *VizieR Online Data Catalog: VII/258*
- Voges, W., Aschenbach, B., Boller, T., et al. 1999, *A&A*, **349**, 389
- Voges, W., Aschenbach, B., Boller, T., et al. 2000, *IAU Circ.*, **7432**, 1
- Watson, M. G., Schröder, A. C., Fyfe, D., et al. 2009, *A&A*, **493**, 339
- White, N. E., & Ghosh, P. 1998, *ApJ*, **504**, L31
- Wilkinson, M. I., Kleyna, J. T., Evans, N. W., et al. 2004, *ApJ*, **611**, L21
- Willingale, R., Starling, R. L. C., Beardmore, A. P., Tanvir, N. R., & O'Brien, P. T. 2013, *MNRAS*, **431**, 394
- Zhang, Z., Gilfanov, M., & Bogdán, Á. 2013, *A&A*, **556**, A9
- Zhu, C., Lü, G., Wang, Z., & Wang, N. 2012, *PASP*, **124**, 195

Appendix A: Catalogue of X-ray sources in the field of the Draco dSph spheroidal galaxy detected by *XMM-Newton*

Table A.1. List of detected sources with classification, coordinates, and X-ray properties.

ID No.	Class <sup>†</sup>	RA (J2000)	Dec (J2000)	$r1\sigma$ ( $''$ )	Count rate (0.2–12 keV) ( $\text{cts s}^{-1}$ )	Flux (0.2–12 keV) ( $\text{erg s}^{-1} \text{cm}^{-2}$ )	ML	HR1	HR2	HR3	HR4
1		17 18 46.52	+57 54 46.5	1.16	4.18e-3 ± 6.64e-4	2.09e-14 ± 3.92e-15	1.15e+1	–	–	–	–
2		17 18 48.45	+57 50 13.3	1.05	5.95e-3 ± 9.47e-4	2.56e-14 ± 5.02e-15	1.47e+1	–	–	–	–
3		17 18 49.99	+57 54 52.9	0.88	4.71e-3 ± 6.57e-4	8.01e-15 ± 3.90e-15	4.03e+1	–	–	–	–
4	GLX	17 18 56.89	+57 51 04.0	1.07	3.34e-3 ± 7.41e-4	4.34e-15 ± 6.46e-15	2.50e+1	–	–	–	–
5	GLX	17 19 00.63	+57 51 45.7	1.19	5.01e-3 ± 6.43e-4	2.04e-14 ± 9.55e-15	6.45e+1	0.43 ± 0.19	0.14 ± 0.15	–0.58 ± 0.18	–
6	AGN	17 19 01.51	+58 00 29.0	0.35	1.19e-2 ± 5.14e-4	8.77e-14 ± 8.85e-15	1.23e+3	0.45 ± 0.13	0.25 ± 0.10	–0.24 ± 0.10	–0.25 ± 0.18
7	AGN	17 19 04.05	+58 03 29.3	1.15	6.51e-3 ± 5.21e-4	3.66e-14 ± 1.03e-14	3.74e+2	0.01 ± 0.20	–0.62 ± 0.24	0.38 ± 0.37	–0.25 ± 0.51
8	GLX	17 19 04.54	+57 47 27.5	0.48	6.67e-3 ± 4.72e-4	4.18e-14 ± 9.42e-15	4.82e+2	0.07 ± 0.14	0.09 ± 0.13	–0.14 ± 0.14	–
9		17 19 06.76	+57 55 48.0	0.92	2.37e-3 ± 5.22e-4	1.43e-14 ± 9.55e-15	2.32e+1	–	–	–	–
10	GLX	17 19 10.33	+57 49 48.0	0.37	1.04e-2 ± 4.88e-4	1.33e-13 ± 1.10e-14	7.32e+2	–	–	–0.17 ± 0.08	–0.16 ± 0.12
11		17 19 11.75	+57 47 20.9	2.44	3.80e-3 ± 8.93e-4	7.22e-15 ± 9.79e-15	1.14e+1	–	–	–	–
12	AGN (r)	17 19 19.62	+57 59 42.2	0.39	6.31e-3 ± 3.15e-4	1.08e-13 ± 8.43e-15	5.87e+2	–	–	0.23 ± 0.20	–0.01 ± 0.22
13	GLX (r)	17 19 20.17	+57 54 01.5	1.30	2.51e-3 ± 3.81e-4	1.24e-14 ± 5.01e-15	5.39e+1	–	–	–	–
14	XRB-CAN	17 19 21.71	+57 49 43.8	0.33	1.00e-2 ± 4.44e-4	6.14e-14 ± 6.43e-15	1.27e+3	–	–	–	–
15		17 19 24.84	+57 44 52.0	0.54	5.96e-3 ± 4.98e-4	3.05e-14 ± 6.97e-15	2.66e+2	–	–	–	–
16	FG	17 19 25.98	+57 50 19.1	1.39	2.43e-3 ± 4.02e-4	3.32e-15 ± 2.11e-15	1.45e+1	–	–	–	–
17		17 19 26.14	+58 00 57.3	1.90	5.63e-3 ± 9.45e-4	1.19e-14 ± 1.04e-14	1.14e+1	–	–	–	–
18	AGN-CAN	17 19 28.02	+57 43 12.6	0.72	4.76e-3 ± 5.89e-4	4.23e-14 ± 1.81e-14	8.94e+1	–	–	0.21 ± 0.27	–
19		17 19 29.56	+57 49 36.4	1.88	3.93e-3 ± 9.64e-4	1.30e-14 ± 8.53e-15	1.59e+1	–	–0.10 ± 0.27	–	–
20	AGN	17 19 34.35	+57 58 50.1	0.17	2.32e-2 ± 5.51e-4	1.53e-13 ± 8.16e-15	6.77e+3	0.12 ± 0.09	0.07 ± 0.08	–0.57 ± 0.08	–0.2 ± 0.21
21	H	17 19 36.65	+57 49 00.2	0.78	7.08e-3 ± 8.84e-4	2.83e-14 ± 9.67e-15	8.43e+1	–0.12 ± 0.22	0.17 ± 0.22	–	–
22		17 19 37.01	+57 46 58.7	0.66	6.96e-3 ± 5.93e-4	1.97e-14 ± 4.62e-15	1.82e+2	0.57 ± 0.18	–0.18 ± 0.18	–	–
23		17 19 45.43	+57 52 56.9	0.56	2.21e-3 ± 1.76e-4	1.24e-14 ± 2.15e-15	2.04e+2	0.62 ± 0.16	–0.13 ± 0.17	–0.06 ± 0.23	–0.56 ±
24	XRB-CAN	17 19 53.96	+57 59 50.8	0.36	5.20e-3 ± 2.41e-4	9.22e-14 ± 6.16e-15	6.96e+2	–	–	0.14 ± 0.10	–0.20 ± 0.12
25	H	17 19 56.21	+58 05 27.1	1.16	4.92e-3 ± 8.91e-4	1.93e-14 ± 1.00e-14	1.83e+1	–	–	–0.01 ± 0.27	–
26		17 19 57.05	+57 46 17.8	0.64	5.37e-3 ± 4.42e-4	2.82e-14 ± 5.73e-15	2.07e+2	–	–	–	–
27	SYM	17 19 57.76	+57 50 06.2	0.88	4.40e-3 ± 2.83e-4	1.03e-14 ± 2.46e-15	1.14e+1	–	–	–	–
28	H	17 20 02.29	+57 55 44.3	0.97	3.05e-3 ± 4.69e-4	4.85e-15 ± 2.09e-15	1.55e+1	–0.12 ± 0.26	0.14 ± 0.25	–	–
29		17 20 08.31	+57 58 20.4	1.07	2.31e-3 ± 3.00e-4	1.29e-14 ± 4.07e-15	4.65e+1	–	–	–	–
30	H	17 20 10.16	+57 54 06.5	1.52	3.07e-3 ± 6.29e-4	7.43e-15 ± 3.05e-15	1.66e+1	–	0.27 ± 0.22	–0.28 ± 0.22	–
31	BS-CAN	17 20 13.92	+57 50 52.4	2.20	2.33e-3 ± 3.38e-4	1.46e-14 ± 4.40e-15	1.96e+1	–	0.19 ± 0.22	–	–
32		17 20 14.67	+57 46 06.5	1.83	3.71e-3 ± 9.68e-4	6.91e-15 ± 7.00e-15	1.72e+1	–	–	–	–
33	BS-CAN	17 20 17.96	+57 51 04.4	0.66	3.37e-3 ± 2.29e-4	1.23e-14 ± 2.29e-15	5.57e+2	0.38 ± 0.08	0.20 ± 0.07	–0.50 ± 0.06	–
34	AGN-CAN	17 20 21.20	+57 43 59.3	2.69	4.02e-3 ± 7.32e-4	5.36e-14 ± 1.65e-14	2.68e+1	–	–	–	–
35	FG	17 20 21.88	+57 58 26.5	0.04	2.22e-1 ± 1.24e-3	9.63e-13 ± 6.24e-15	1.87e+5	0.61 ± 0.01	–0.21 ± 0.01	–0.72 ± 0.01	–0.69 ± 0.03
36	AGN-CAN	17 20 21.70	+57 43 27.6	0.71	6.91e-3 ± 6.91e-4	2.97e-14 ± 8.13e-15	1.68e+2	–	–	–	–
37	H	17 20 23.57	+57 50 09.1	2.22	3.07e-3 ± 7.90e-4	1.20e-14 ± 6.89e-15	1.73e+1	–	–	0.04 ± 0.27	–
38	H	17 20 25.77	+57 52 41.3	1.77	3.20e-3 ± 7.61e-4	1.68e-14 ± 7.31e-15	1.00e+1	–	0.51 ± 0.36	–	–
39	FG	17 20 25.64	+57 53 04.4	0.65	2.37e-3 ± 2.40e-4	6.65e-15 ± 2.15e-15	1.66e+2	0.53 ± 0.24	–	–	–
40		17 20 28.33	+57 56 23.3	0.63	2.30e-3 ± 2.64e-4	1.05e-14 ± 2.93e-15	7.13e+1	0.06 ± 0.21	–0.32 ± 0.17	–	–

Notes. <sup>(†)</sup> GLX: galaxy, AGN: active galactic nuclei, FG: foreground star, XRB: X-ray binary, SYM: symbiotic star, BS: binary system, H: hard source, CAN: candidate, (r): source with radio counterpart.

Table A.1. continued.

ID No.	Class <sup>†</sup>	RA (J2000)	Dec (J2000)	$r\sigma$ ( $''$ )	Count rate (0.2–12 keV) (cts $s^{-1}$ )	Flux (0.2–12 keV) (ergs $s^{-1}$ cm $^{-2}$ )	ML	HR1	HR2	HR3	HR4
41	GLX-CAN	17 20 32.86	+58 07 16.0	1.85	1.09e-2 $\pm$ 2.72e-3	6.50e-14 $\pm$ 3.89e-14	2.14e+1	–	–	–	–
42	GLX-CAN	17 20 33.08	+58 06 13.7	2.03	5.83e-3 $\pm$ 1.15e-3	5.32e-14 $\pm$ 2.50e-14	4.29e+1	–	-0.59 $\pm$ 0.36	–	–
43	AGN	17 20 33.62	+58 08 29.7	0.23	9.60e-2 $\pm$ 1.85e-3	6.66e-13 $\pm$ 2.84e-14	1.29e+4	-0.05 $\pm$ 0.075	0.02 $\pm$ 0.07	-0.41 $\pm$ 0.08	-0.24 $\pm$ 0.18
44	AGN	17 20 37.10	+57 48 56.3	0.33	8.80e-3 $\pm$ 3.54e-4	1.07e-13 $\pm$ 8.69e-15	1.25e+3	-0.35 $\pm$ 0.09	-0.26 $\pm$ 0.14	0.30 $\pm$ 0.14	–
45	FG	17 20 37.62	+58 02 12.4	0.11	5.88e-2 $\pm$ 8.16e-4	2.49e-13 $\pm$ 7.19e-15	2.16e+4	0.55 $\pm$ 0.02	-0.05 $\pm$ 0.02	-0.61 $\pm$ 0.03	-0.72 $\pm$ 0.07
46		17 20 38.45	+57 45 45.4	1.22	4.36e-3 $\pm$ 9.78e-4	1.63e-14 $\pm$ 1.10e-14	2.49e+1	–	–	–	–
47	H	17 20 39.66	+57 56 48.8	1.62	3.03e-3 $\pm$ 8.10e-4	1.27e-14 $\pm$ 8.30e-15	1.14e+1	–	–	0.03 $\pm$ 0.29	–
48	AGN-CAN	17 20 43.08	+57 54 43.2	0.35	5.33e-3 $\pm$ 2.35e-4	6.78e-14 $\pm$ 5.12e-15	7.59e+2	0.74 $\pm$ 0.15	0.39 $\pm$ 0.10	-0.24 $\pm$ 0.08	-0.15 $\pm$ 0.12
49	H	17 20 47.27	+57 53 20.6	0.64	3.09e-3 $\pm$ 2.69e-4	2.15e-14 $\pm$ 4.28e-15	1.52e+2	–	–	–	–
50	AGN-CAN	17 20 51.94	+57 41 59.0	0.41	2.18e-2 $\pm$ 1.02e-3	2.09e-13 $\pm$ 2.17e-14	9.77e+2	–	0.45 $\pm$ 0.071	-0.24 $\pm$ 0.07	–
51	AGN(r)	17 20 52.28	+57 55 13.2	0.17	2.30e-2 $\pm$ 4.65e-4	1.95e-13 $\pm$ 7.67e-15	6.86e+3	0.18 $\pm$ 0.06	0.07 $\pm$ 0.06	-0.25 $\pm$ 0.06	–
52		17 20 52.50	+58 04 51.1	1.05	7.90e-3 $\pm$ 2.43e-3	3.26e-14 $\pm$ 3.13e-14	1.53e+1	–	-0.15 $\pm$ 0.27	–	–
53	GLX-CAN	17 20 56.35	+57 47 41.7	1.01	3.62e-3 $\pm$ 6.07e-4	1.75e-14 $\pm$ 3.66e-15	1.36e+1	–	–	–	–
54	AGN-CAN	17 21 00.45	+57 51 53.5	0.66	4.88e-3 $\pm$ 5.10e-4	1.42e-14 $\pm$ 5.19e-15	1.18e+2	–	0.32 $\pm$ 0.21	–	–
55	AGN-CAN	17 21 04.38	+57 41 06.0	0.83	1.72e-2 $\pm$ 1.61e-3	6.28e-14 $\pm$ 1.91e-14	1.22e+2	0.19 $\pm$ 0.21	-0.05 $\pm$ 0.19	–	–
56		17 21 05.04	+57 53 38.2	2.07	1.95e-3 $\pm$ 4.51e-4	1.28e-14 $\pm$ 6.87e-15	8.96e+1	–	–	–	–
57		17 21 12.02	+57 50 01.5	0.80	4.56e-3 $\pm$ 7.49e-4	2.30e-14 $\pm$ 1.17e-14	7.58e+1	–	–	–	–
58	H	17 21 13.06	+57 56 15.2	0.87	4.10e-3 $\pm$ 5.95e-4	1.96e-14 $\pm$ 8.23e-15	3.79e+1	–	–	0.09 $\pm$ 0.23	–
59	FG	17 21 16.66	+58 01 16.5	1.95	6.07e-3 $\pm$ 1.17e-3	8.20e-15 $\pm$ 1.24e-14	3.20e+1	0.51 $\pm$ 0.18	–	–	–
60	AGN	17 21 22.92	+57 50 29.2	0.61	9.40e-3 $\pm$ 8.57e-4	6.56e-14 $\pm$ 1.43e-14	1.94e+2	-0.43 $\pm$ 0.10	-0.11 $\pm$ 0.17	-0.02 $\pm$ 0.21	–
61		17 21 24.66	+57 52 53.6	2.23	1.11e-2 $\pm$ 4.25e-3	5.03e-14 $\pm$ 4.96e-14	1.14e+1	–	–	–	–
62		17 21 29.13	+57 47 08.9	1.80	7.09e-3 $\pm$ 1.76e-3	6.17e-14 $\pm$ 2.80e-14	1.14e+1	–	–	–	–
63		17 21 36.11	+58 03 02.2	1.77	5.48e-3 $\pm$ 1.20e-3	8.40e-15 $\pm$ 1.20e-14	1.14e+1	0.21 $\pm$ 0.25	–	–	–
64	XRB-CAN	17 21 39.51	+58 01 45.2	0.87	8.88e-3 $\pm$ 1.78e-3	2.92e-14 $\pm$ 2.06e-14	5.59e+1	0.91 $\pm$ 0.18	–	–	–
65	XRB-CAN	17 21 40.60	+58 02 44.8	1.63	1.39e-2 $\pm$ 2.21e-3	9.51e-14 $\pm$ 3.12e-14	1.14e+1	–	0.04 $\pm$ 0.28	–	–
66	GLX-CAN	17 21 41.08	+57 45 53.2	1.61	8.99e-3 $\pm$ 2.81e-3	1.88e-14 $\pm$ 3.24e-14	1.86e+1	–	–	0.31 $\pm$ 0.25	–
67	AGN-CAN	17 21 41.40	+57 52 35.2	0.66	7.35e-3 $\pm$ 7.36e-4	3.38e-14 $\pm$ 8.91e-15	2.48e+2	0.24 $\pm$ 0.20	-0.13 $\pm$ 0.22	–	–
68	AGN	17 21 48.46	+57 58 03.2	0.72	8.52e-3 $\pm$ 8.20e-4	3.84e-14 $\pm$ 1.34e-14	1.99e+2	0.41 $\pm$ 0.21	–	–	–
69	FG	17 21 58.32	+57 49 22.7	0.11	8.55e-1 $\pm$ 1.81e-2	1.82e-12 $\pm$ 9.29e-14	3.76e+4	0.27 $\pm$ 0.02	-0.13 $\pm$ 0.02	-0.54 $\pm$ 0.03	-0.61 $\pm$ 0.08
70	AGN	17 22 11.69	+57 56 51.1	1.88	1.24e-2 $\pm$ 1.71e-3	5.06e-14 $\pm$ 2.18e-14	3.44e+1	-0.17 $\pm$ 0.25	0.18 $\pm$ 0.24	–	–

**Table A.2.** Optical counterparts from the SDSS9 catalogue.

ID	Class	SDSS9 ID	$g$ (mag)	$r$ (mag)	$i$ (mag)	$\log_{10}(\frac{F_x}{F_{opt}})$
1		–	–	–	–	–
2		–	–	–	–	–
3		J171850.16+575453.0	$21.74 \pm 0.09$	$20.86 \pm 0.06$	$21.11 \pm 0.14$	$-0.03 \pm 0.21$
4	GLX	J171856.97+575102.5	$18.10 \pm 0.01$	$16.96 \pm 0.01$	$16.52 \pm 0.01$	$-1.75 \pm 0.64$
5	GLX	J171900.84+575147.0	$20.27 \pm 0.02$	$19.57 \pm 0.01$	$19.18 \pm 0.02$	$-0.21 \pm 0.20$
6	AGN	J171901.68+580028.9	$18.79 \pm 0.01$	$18.67 \pm 0.01$	$18.68 \pm 0.01$	$-0.17 \pm 0.04$
7	AGN	J171904.16+580329.3	$20.35 \pm 0.02$	$20.33 \pm 0.02$	$20.29 \pm 0.04$	$0.07 \pm 0.12$
8	GLX	J171904.62+574728.1	$20.49 \pm 0.02$	$19.55 \pm 0.02$	$19.12 \pm 0.02$	$0.18 \pm 0.09$
9		–	–	–	–	–
10	GLX	J171910.45+574948.0	$18.96 \pm 0.01$	$18.00 \pm 0.01$	$17.45 \pm 0.01$	$0.07 \pm 0.03$
11		J171910.90+574718.1	$23.71 \pm 0.2$	$22.00 \pm 0.10$	$21.67 \pm 0.12$	$0.71 \pm 0.58$
12	AGN (r)	–	–	–	–	–
13	AGN (r)	J171919.93+575401.3	$15.94 \pm 0.00$	$15.11 \pm 0.01$	$14.68 \pm 0.01$	$-2.15 \pm 0.17$
14	XRB-CAN	J171921.82+574943.7	$22.76 \pm 0.13$	$22.48 \pm 0.15$	$21.68 \pm 0.12$	$1.26 \pm 0.04$
15		–	–	–	–	–
16	FG	J171925.97+575020.1	$14.74 \pm 0.01$	$14.52 \pm 0.01$	$12.38 \pm 0.01$	$-3.21 \pm 0.27$
17		J171925.68+580100.3	$19.39 \pm 0.01$	$18.67 \pm 0.01$	$18.37 \pm 0.01$	$-0.79 \pm 0.37$
18	AGN-CAN	J171928.00+574313.3	$20.85 \pm 0.03$	$20.76 \pm 0.04$	$20.42 \pm 0.04$	$0.33 \pm 0.18$
19		–	–	–	–	–
20	AGN	J171934.41+575849.6	$19.34 \pm 0.01$	$19.27 \pm 0.01$	$19.02 \pm 0.01$	$0.29 \pm 0.02$
21	H	–	–	–	–	–
22		J171936.97+574659.0	$22.84 \pm 0.14$	$21.84 \pm 0.09$	$21.35 \pm 0.09$	$0.80 \pm 0.10$
23		J171945.41+575257.3	$22.93 \pm 0.18$	$21.47 \pm 0.06$	$21.56 \pm 0.11$	$0.63 \pm 0.07$
24	XRB-CAN	J171954.02+575951.3	$22.96 \pm 0.20$	$22.27 \pm 0.15$	$21.88 \pm 0.16$	$1.52 \pm 0.02$
25	H	–	–	–	–	–
26		–	–	–	–	–
27	SYM	J171957.64+575005.7	$17.75 \pm 0.01$	$16.47 \pm 0.01$	$16.19 \pm 0.01$	$-1.51 \pm 0.10$
28	H	–	–	–	–	–
29		–	–	–	–	–
30	H	J172010.50+575404.9	$22.45 \pm 0.13$	$23.05 \pm 0.29$	$23.04 \pm 0.46$	$0.22 \pm 0.17$
31	BS-CAN	J172013.37+575051.9	$18.61 \pm 0.01$	$17.74 \pm 0.01$	$17.38 \pm 0.01$	$-1.02 \pm 0.13$
32		J172015.25+574604.7	$22.28 \pm 0.10$	$21.94 \pm 0.10$	$21.77 \pm 0.14$	$0.12 \pm 0.44$
33	BS-CAN	J172018.01+575105.5	$19.48 \pm 0.01$	$17.98 \pm 0.01$	$16.84 \pm 0.01$	$-0.74 \pm 0.08$
34	AGN-CAN	J172021.04+574401.4	$21.56 \pm 0.05$	$21.17 \pm 0.05$	$20.87 \pm 0.06$	$0.72 \pm 0.13$
35	FG	J172021.83+575827.3	$12.80 \pm 0.01$	$12.79 \pm 0.01$	$11.81 \pm 0.01$	$-1.52 \pm 0.01$
36	AGN-CAN	J172021.63+574327.0	$21.34 \pm 0.04$	$21.14 \pm 0.04$	$20.8 \pm 0.06$	$0.37 \pm 0.11$
37	H	J172023.92+575009.9	$24.27 \pm 0.48$	$24.50 \pm 0.62$	$24.19 \pm 0.70$	$1.16 \pm 0.24$
38	H	–	–	–	–	–
39	FG	J172025.65+575304.4	$11.82 \pm 0.01$	$14.19 \pm 0.01$	$11.34 \pm 0.01$	$-4.07 \pm 0.14$
40		–	–	–	–	–
41	GLX-CAN	J172033.09+580714.9	$22.60 \pm 0.16$	$21.80 \pm 0.11$	$20.91 \pm 0.08$	$1.22 \pm 0.25$
42	GLX-CAN	J172033.71+580612.6	$24.12 \pm 0.57$	$22.26 \pm 0.17$	$21.66 \pm 0.16$	$1.74 \pm 0.20$
43	AGN	J172033.61+580829.7	$17.33 \pm 0.01$	$16.66 \pm 0.01$	$16.24 \pm 0.01$	$0.12 \pm 0.01$
44	AGN	J172037.13+574856.3	$19.32 \pm 0.01$	$18.64 \pm 0.01$	$18.27 \pm 0.01$	$0.12 \pm 0.03$
45	FG	J172037.64+580211.9	$11.39 \pm 0.01$	$13.95 \pm 0.01$	$12.98 \pm 0.01$	$-2.67 \pm 0.01$
46		–	–	–	–	–
47	H	–	–	–	–	–
48	AGN-CAN	J172043.09+575443.2	$20.92 \pm 0.03$	$20.44 \pm 0.03$	$20.21 \pm 0.03$	$0.57 \pm 0.03$
49	H	–	–	–	–	–
50	AGN-CAN	J172051.91+574159.7	$19.84 \pm 0.01$	$19.89 \pm 0.02$	$19.72 \pm 0.02$	$0.62 \pm 0.04$
51	AGN (r)	J172052.30+575513.4	$20.28 \pm 0.02$	$19.99 \pm 0.02$	$19.95 \pm 0.03$	$0.77 \pm 0.01$
52		–	–	–	–	–
53	GLX-CAN	J172056.48+574739.6	$24.23 \pm 0.58$	$22.35 \pm 0.18$	$21.14 \pm 0.10$	$1.31 \pm 0.09$
54	AGN-CAN	J172100.52+575152.9	$21.44 \pm 0.05$	$21.51 \pm 0.07$	$21.52 \pm 0.15$	$0.10 \pm 0.15$
55	AGN-CAN	J172104.23+574106.2	$20.58 \pm 0.02$	$20.73 \pm 0.03$	$20.56 \pm 0.05$	$0.40 \pm 0.13$
56		J172104.75+575335.1	$15.97 \pm 0.01$	$15.30 \pm 0.01$	$15.03 \pm 0.01$	$-2.13 \pm 0.23$
57*		J172112.06+575002.0	$20.58 \pm 0.03$	$20.88 \pm 0.04$	$22.80 \pm 0.35$	$-0.03 \pm 0.22$

**Notes.** ID: ID number of *XMM-Newton* source. SDSS9 ID: ID number of the optical source according to the SDSS9 catalogue. Source class: source class is the same as Table A.1.  $g$ ,  $r$ ,  $i$ : apparent magnitudes of the counterparts in different optical energy bands of SDSS9. The extinction was applied for the magnitude according to [Schlafly & Finkbeiner \(2011\)](#). (\*) For source No. 57, data were taken from SDSS7 (see Sect. 3.2).

Table A.2. continued.

ID	Class	SDSS9 ID	$g$ (mag)	$r$ (mag)	$i$ (mag)	$\log_{10}(\frac{F_x}{F_{opt}})$
58	H	–	–	–	–	–
59	FG	J172116.97+580113.6	$11.66 \pm 0.01$	$13.67 \pm 0.01$	$14.55 \pm 0.01$	$-4.04 \pm 0.65$
60	AGN	J172122.81+575029.6	$18.04 \pm 0.01$	$18.01 \pm 0.01$	$17.81 \pm 0.01$	$-0.59 \pm 0.09$
61		J172124.61+575253.6	$20.35 \pm 0.02$	$19.99 \pm 0.02$	$19.87 \pm 0.02$	$0.21 \pm 0.42$
62		–	–	–	–	–
63		–	–	–	–	–
64	XRB-CAN	J172139.48+580145.1	$23.73 \pm 0.30$	$23.16 \pm 0.29$	$22.20 \pm 0.21$	$1.32 \pm 0.30$
65	XRB-CAN	–	–	–	–	–
66	GLX-CAN	J172141.18+574555.6	$23.12 \pm 0.23$	$22.43 \pm 0.18$	$22.52 \pm 0.33$	$0.89 \pm 0.74$
67	AGN-CAN	J172141.43+575235.5	$21.53 \pm 0.05$	$21.12 \pm 0.06$	$20.69 \pm 0.05$	$0.51 \pm 0.11$
68	AGN	J172148.27+575805.3	$20.19 \pm 0.01$	$20.09 \pm 0.02$	$19.73 \pm 0.02$	$0.03 \pm 0.15$
69	FG	J172158.29+574922.5	$11.21 \pm 0.01$	$13.03 \pm 0.01$	$10.1 \pm 0.01$	$-1.88 \pm 0.02$
70	AGN	J172211.64+575652.1	$20.50 \pm 0.02$	$20.37 \pm 0.03$	$20.14 \pm 0.03$	$0.27 \pm 0.18$

**Appendix B: Long-term light curves**

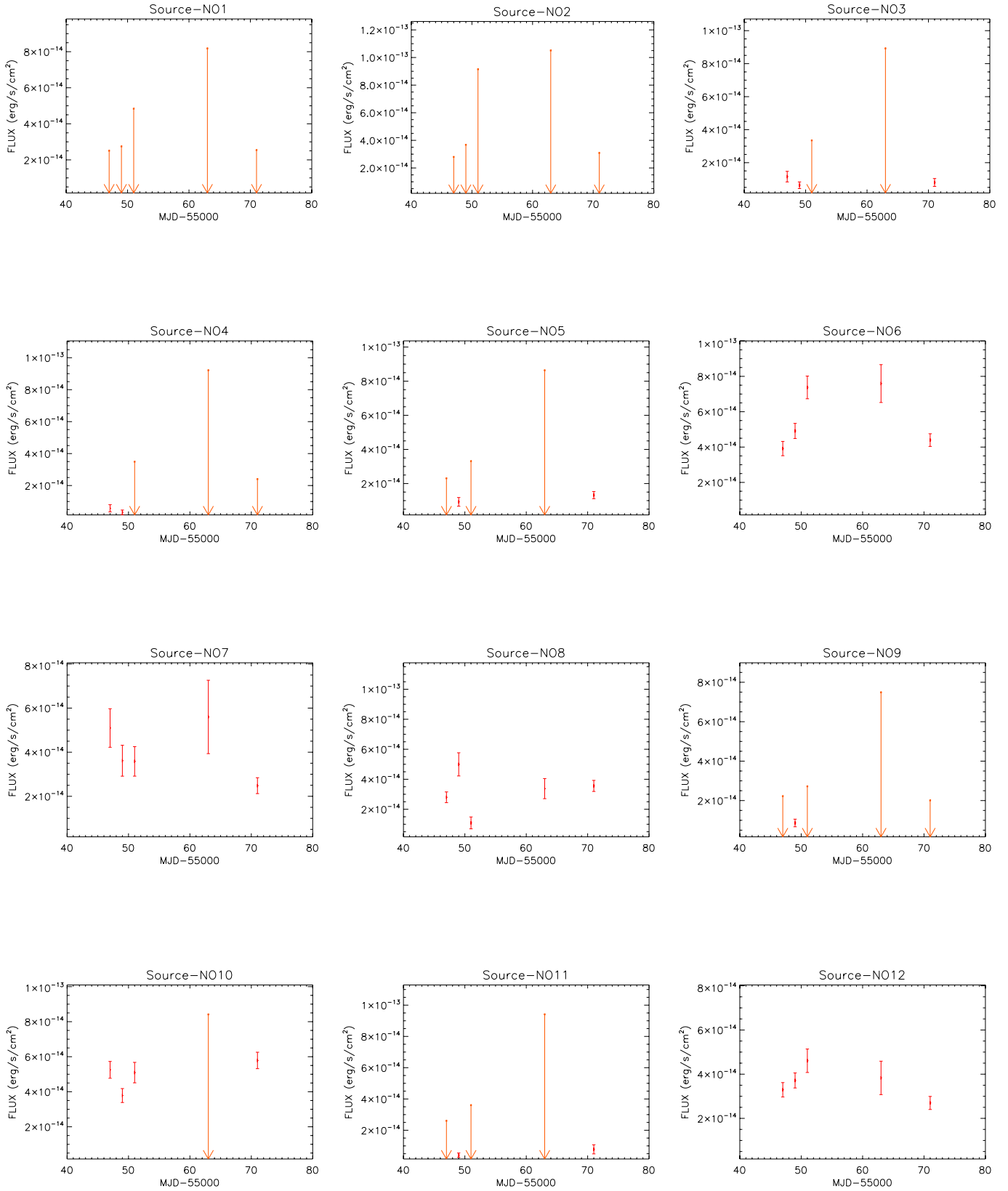


**Fig. B.1.** Light curve of each source over five observations. The weighted (0.2–4.5 keV) flux of each source in different observations is plotted over time. If the source was not detected in an observation, the upper limit was calculated.

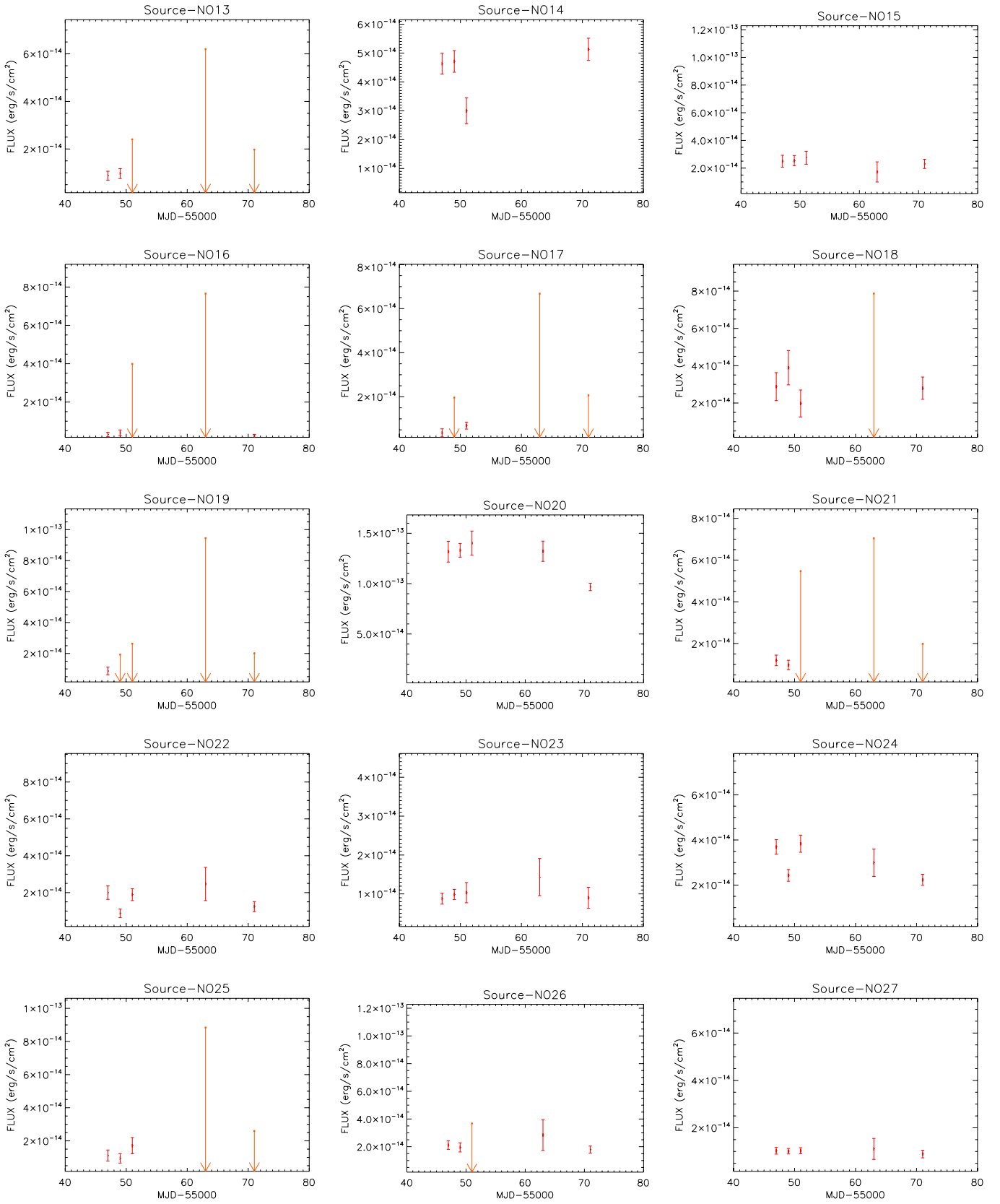


Fig. B.1. continued.

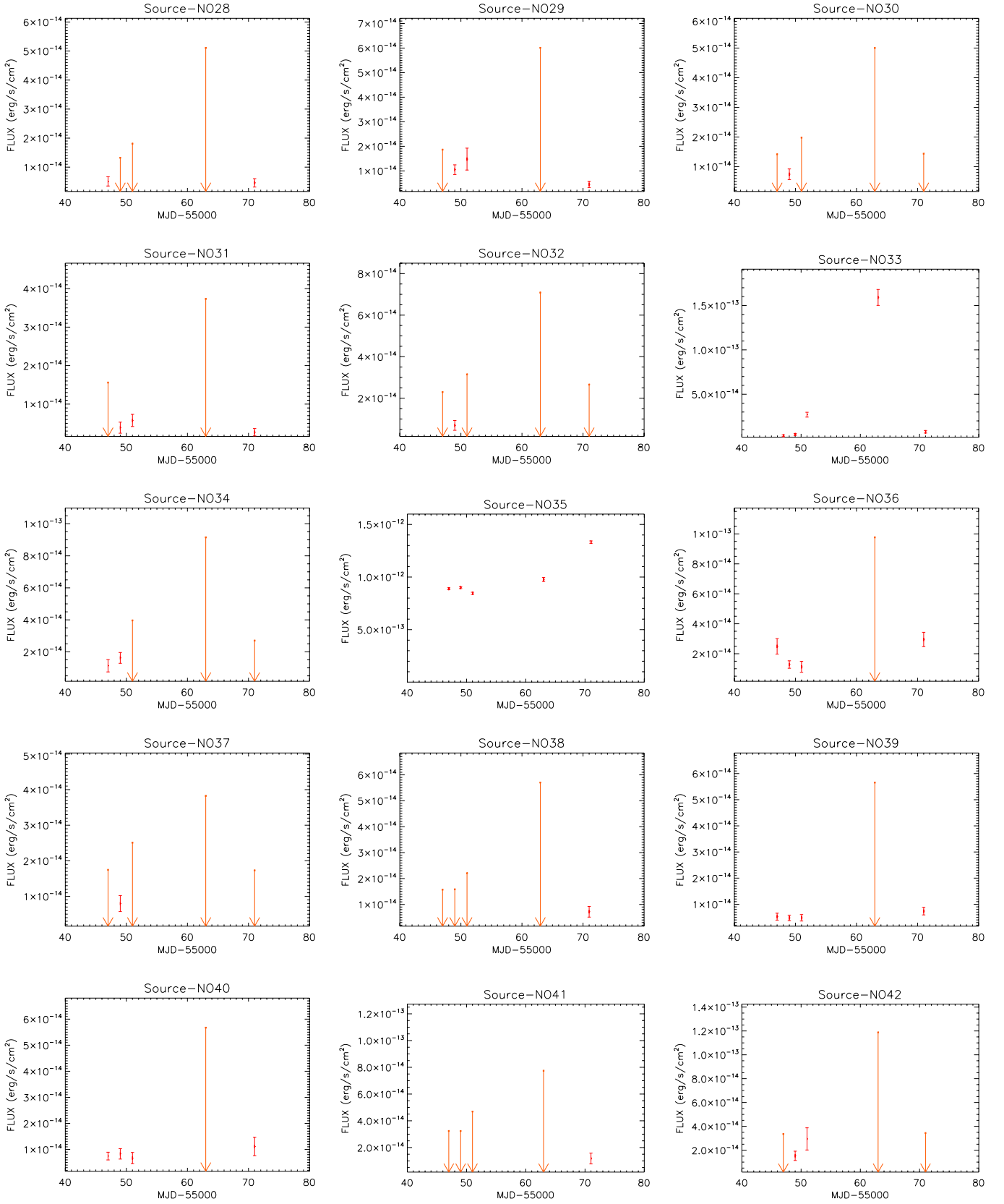


Fig. B.1. continued.

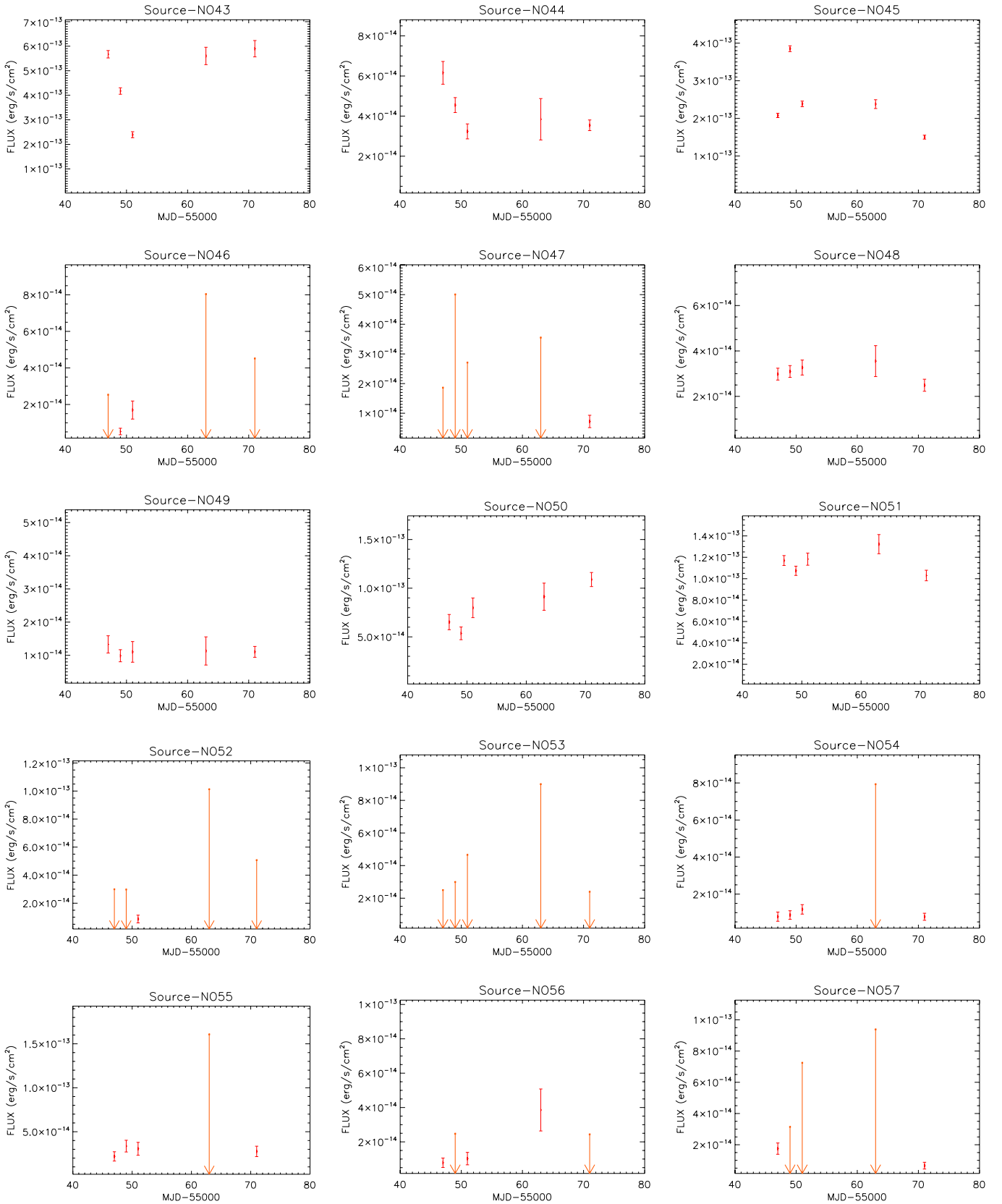


Fig. B.1. continued.

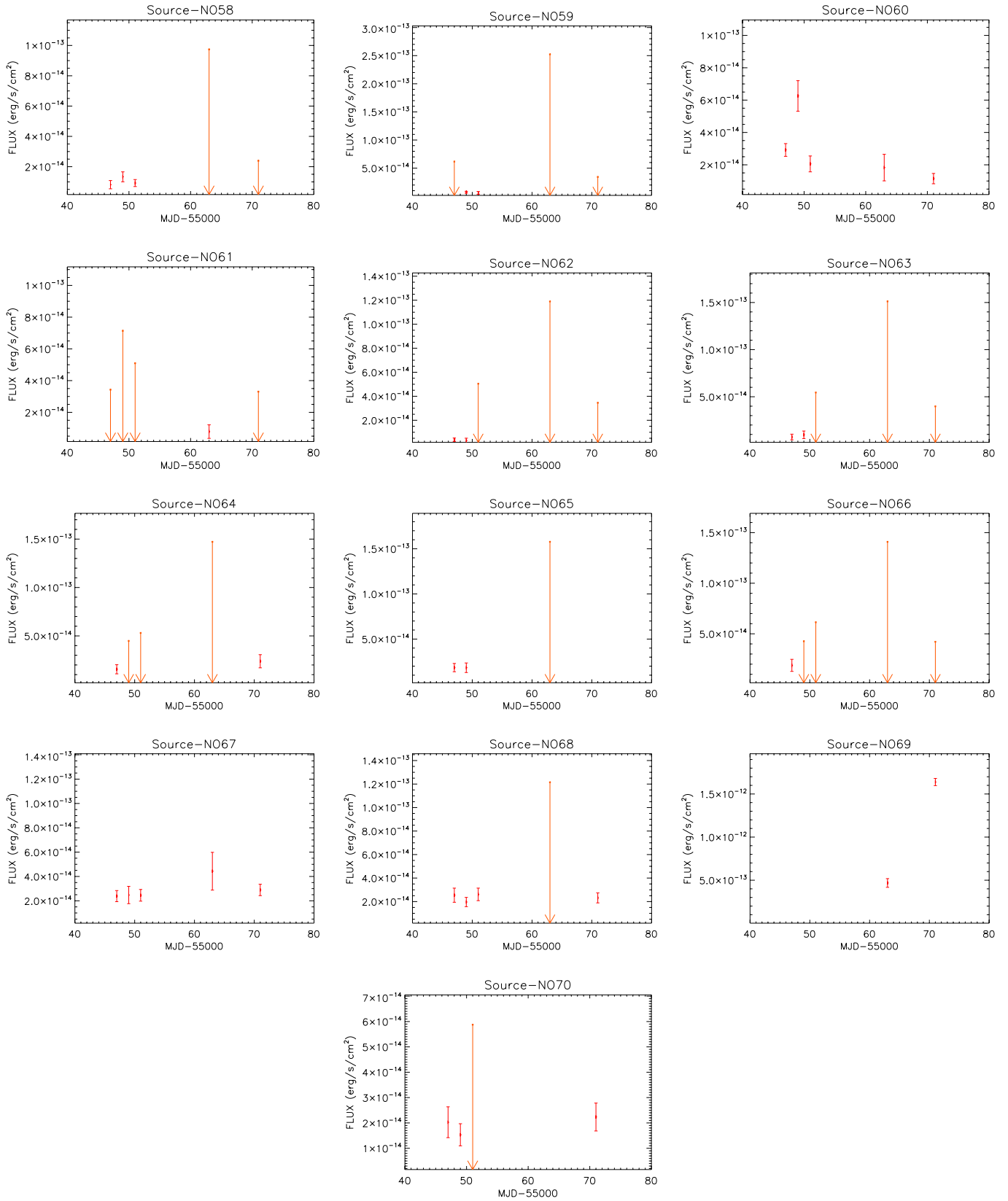


Fig. B.1. continued.